

**THE EXPERIMENTAL STUDY OF AERODYNAMIC CHARACTERISTICS WITH
WING FLEXIBILITY FOR HAWKMOTH-LIKE WINGS IN HOVERING FLIGHT**

by

YeongGyun Ryu, B. Eng
Aerospace Engineering
Ryerson University, 2012

A thesis, presented by Ryerson University

In partial fulfillment of the requirements for the degree of

Master of Science

In the program of Aerospace Engineering

Toronto, Ontario, Canada, 2014

© YeongGyun Ryu 2014

AUTHOR'S DECLARATION FOR ELECTRONIC SUBMISSION OF A THESIS

I hereby declare that I am the sole author of this thesis. This is a true copy of the thesis, including any required final revisions, as accepted by my examiners.

I authorize Ryerson University to lend this thesis to other institutions or individuals for the purpose of scholarly research

I further authorize Ryerson University to reproduce this thesis by photocopying or by other means, in total or in part, at the request of other institutions or individuals for the purpose of scholarly research.

I understand that my thesis may be made electronically available to the public.

THE EXPERIMENTAL STUDY OF AERODYNAMIC CHARACTERISTICS WITH WING
FLEXIBILITY FOR HAWKMOTH-LIKE WINGS IN HOVERING FLIGHT

Master of Science, 2014

YeongGyun Ryu

Aerospace Engineering, Ryerson University

ABSTRACT

An experimental study on flapping wing flexibility in hovering flight has been conducted to investigate the wing flexibility for insect-inspired flapping Micro Aerial Vehicles (MAVs). Hawkmoth-like wing models, derived from *Manduca sexta*, were made of Polycarbonate (PC) sheet with a spanwise length of 200 mm and an aspect ratio of 6.18. For the distributions of wing flexibility, the wing thickness was selected as the design variable: rigid wing (3 mm-thick) and flexible wings (2, 1, 0.8, 0.5, 0.35, 0.2, and 0.1 mm-thick). In the experiment, the wing models were constrained to the symmetrical and sinusoidal flapping motions with sweeping and rotating amplitudes of 120° and 90° in water tank with size of 3.5 m × 1.0 m × 1.1 m. Aerodynamic force and flow structures for flapping the wing were measured using a six-axis force/torque sensor and a high speed camera with a laser using Digital Particle Image Velocimetry (DPIV). To compare the flow structures of flexible wings with rigid wing, they were captured at the same chordwise cross-section as the rigid wing, 50% of wing length. Based on the experimental results, the delay in flapping motion, due to bending and twisting wing, influences the generations of

vortices and aerodynamic force. Consequently, the wing with thickness of 0.8 mm has better aerodynamic characteristics than other wings in hovering flight. This finding will be instrumental in identifying the range of wing flexibilities that improves the aerodynamic efficiency for the development of insect-inspired flapping MAVs.

ACKNOWLEDGEMENT

I would like to express my deepest appreciation to my advisor, Dr. Joon Chung, for his guidance and support as well as his patience and constant encouragement.

I'm grateful to my advisor in Korea Aerospace University, Dr. Jo Won Chang, for the opportunity to conduct aerodynamics experiments in his laboratory.

I owe special thanks to the Ryerson Aerospace Engineering Department for the opportunity to be the Aerospace Engineer.

Finally, I would like to thank to my parents, ByungWook and YoungAe, and my sister, JooYeon, for their constant support and love.

TABLE OF CONTENTS

1	Introduction	1
1.1	Motivation to study insect-inspired flapping air vehicles	1
1.2	Insect flapping flight	2
1.2.1	Experimental studies in insect flapping flight	2
1.2.2	Computational studies in insect flapping flight	3
1.3	Unsteady mechanisms in insect flapping flight.....	4
1.3.1	Leading edge vortex and delayed stall.....	5
1.3.2	Rotational circulation.....	6
1.3.3	Wake-capture (wing-wake interaction).....	7
1.4	Wing flexibility in insect flapping flight.....	8
1.5	Hovering flight	10
1.6	Experiment Facility	11
1.7	Aims and objectives in present study	12
2	Experimental setup and procedure	13
2.1	Wing models	14
2.2	Water tank and experimental motion model	17
2.3	Kinematics.....	19
2.4	Force Measurements	21
2.5	Digital Particle Image Velocimetry (DPIV).....	23
3	Results and discussion	25
3.1	Rigid wing	25
3.1.1	Symmetrical flapping motion	25
3.1.2	Sinusoidal flapping motion.....	31

3.2	Flexible wings	36
3.2.1	Symmetrical flapping motion	36
3.2.2	Sinusoidal flapping motion	44
4	Conclusion and future work	51
4.1	Symmetrical flapping motion vs. Sinusoidal flapping motion.....	51
4.2	Conclusion.....	54
	Reference	57
	Appendices.....	64
A.	Experimental uncertainty	64
B.	Lift and drag coefficient.....	66
i.	Symmetrical Flapping motion.....	66
ii.	Sinusoidal flapping motion	70

LIST OF TABLES

Table 1 Wing data in the present experiment	17
---	----

LIST OF FIGURES

Figure 1.1 Leading edge vortex on hawkmoth wing during downstroke. (a) smoke-visualization [11] (b) computational visualization [10]	3
Figure 1.2 Summary of aerodynamic mechanisms in insect flapping flight, designed by Dickinson, M. H. in “Catching the Wake”, SCIENTIFIC AMERICAN™ [20]	4
Figure 1.3 Flow around a thin airfoil [21]	5
Figure 1.4 Hovering flight of fruit fly [20]	10
Figure 1.5 Dr. Chang’s laboratory in Korea Aerospace University	11
Figure 2.1(a) Real hawkmoth wing (b) Hawkmoth-like wing model used in current experiment. 14	
Figure 2.2 Water tank and Flapping motion coordinates in current experiment	18
Figure 2.3 Experimental Setup: Side-view	19
Figure 2.4 The wing motion sketches: 1. Pitching-down, 2. Constant, 3. Pitching-up, designed by Sun and Tang [12].....	20
Figure 2.5 Flapping wing motions: (a) Symmetrical flapping motion (b) Sinusoidal flapping motion	21
Figure 2.6 Scheme of Force measurement.....	22
Figure 2.7 Definition of force vectors on the wing.....	23
Figure 2.8 Scheme of Digital Particle Image Velocimetry (DPIV) system.....	24
Figure 3.1 Trajectories of symmetrical flapping motion	25
Figure 3.2 Lift and drag coefficients distributions of rigid cases in a symmetrical flapping motion	25

Figure 3.3 Normalized sweeping and rotating velocities each cycle in a symmetrical flapping motion.....	26
Figure 3.4 Lift and drag coefficient distributions of case 1 in a symmetrical flapping motion....	28
Figure 3.5 Time-resolved flow structures of case 1 at 0.5R chordwise cross-section in a symmetrical flapping motion: (a) $t/T = 0.056$, (b) $t/T = 0.1$, (c) $t/T = 0.25$, (d) $t/T = 0.45$, (e) $t/T = 0.55$	29
Figure 3.6 Trajectories of sinusoidal flapping motion.....	31
Figure 3.7 Lift and drag coefficient distributions of rigid cases in a sinusoidal flapping motion	32
Figure 3.8 Normalized sweeping and rotating velocities each cycle in a sinusoidal flapping motion	32
Figure 3.9 Lift and drag coefficient distributions of case 1 in a sinusoidal flapping motion	33
Figure 3.10 Time-resolved flow structures of case 1 at 0.5R chordwise cross-section in a sinusoidal flapping motion: (a) $t/T = 0.056$, (b) $t/T = 0.1$, (c) $t/T = 0.25$, (d) $t/T = 0.304$, (e) $t/T = 0.55$	34
Figure 3.11 Time-resolved lift and drag coefficient distributions, from case 1 to case 8, in a symmetrical flapping motion	36
Figure 3.12 Mean lift and drag coefficients from case 1 to 8 in a symmetrical flapping motion.	37
Figure 3.13 Distributions of lift and drag coefficients for case 1, 4, 5, and 6 in a symmetrical flapping motion.....	38
Figure 3.14 Sketches of side views for 0.5R chordwise cross-sectional DPIV test in a symmetrical flapping motion; (a) at $t/T = 0.05$ (b) at $t/T = 0.25$	39
Figure 3.15 Time-resolved flow structures at 0.5R chordwise cross-section in a symmetrical flapping motion: (a) at $t/T = 0.05, 0.1, 0.25, 0.45$	41

Figure 3.16 Time-resolved lift and drag coefficient distributions, from case 1 to case 8, in a sinusoidal flapping motion.....	44
Figure 3.17 Mean lift and drag coefficients from case 1 to 8 in a sinusoidal flapping motion	45
Figure 3.18 Distributions of lift and drag coefficients for case 1, 4, 5, and 6 in a sinusoidal flapping motion	46
Figure 3.19 Sketches of side views for 0.5R chordwise cross-sectional DPIV test in a sinusoidal flapping motion; (a) at $t/T = 0.056$ (b) at $t/T = 0.25$	47
Figure 3.20 Time-resolved flow structures at 0.5R chordwise cross-section in a sinusoidal flapping motion: (a) at $t/T = 0.056, 0.1, 0.25, 0.304$	48
Figure 4.1 DPIV results for case 1 in both symmetrical and sinusoidal flapping motions.....	52
Figure 4.2 $CL_{1.5}/CD$, from case 1 to 8, in symmetrical and sinusoidal flapping motions	53
Appendix Fig. 1 Lift and drag coefficients: case 1 (3 mm-thick) vs. case 2 (2 mm-thick), in a symmetrical flapping motion	66
Appendix Fig. 2 Lift and drag coefficients: case 1 (3 mm-thick) vs. case 3 (1 mm-thick), in a symmetrical flapping motion	66
Appendix Fig. 3 Lift and drag coefficients: case 1 (3 mm-thick) vs. case 4 (0.8 mm-thick), in a symmetrical flapping motion	67
Appendix Fig. 4 Lift and drag coefficients: case 1 (3 mm-thick) vs. case 5 (0.5 mm-thick), in a symmetrical flapping motion	67
Appendix Fig. 5 Lift and drag coefficients: case 1 (3 mm-thick) vs. case 6 (0.35 mm-thick), in a symmetrical flapping motion	68
Appendix Fig. 6 Lift and drag coefficients: case 1 (3 mm-thick) vs. case 7 (0.2 mm-thick), in a symmetrical flapping motion	68

Appendix Fig. 7 Lift and drag coefficients: case 1 (3 mm-thick) vs. case 8 (0.1 mm-thick), in a symmetrical flapping motion 69

Appendix Fig. 8 Lift and drag coefficients: case 1 (3 mm-thick) vs. case 2 (2 mm-thick), in a sinusoidal flapping motion..... 70

Appendix Fig. 9 Lift and drag coefficients: case 1 (3 mm-thick) vs. case 3 (1 mm-thick), in a sinusoidal flapping motion..... 70

Appendix Fig. 10 Lift and drag coefficients: case 1 (3 mm-thick) vs. case 4 (0.8 mm-thick), in a sinusoidal flapping motion..... 71

Appendix Fig. 11 Lift and drag coefficients: case 1 (3 mm-thick) vs. case 5 (0.5 mm-thick), in a sinusoidal flapping motion..... 71

Appendix Fig. 12 Lift and drag coefficients: case 1 (3 mm-thick) vs. case 6 (0.35 mm-thick), in a sinusoidal flapping motion..... 72

Appendix Fig. 13 Lift and drag coefficients: case 1 (3 mm-thick) vs. case 7 (0.2 mm-thick), in a sinusoidal flapping motion..... 72

Appendix Fig. 14 Lift and drag coefficients: case 1 (3 mm-thick) vs. case 8 (0.1 mm-thick), in a sinusoidal flapping motion..... 73

NOMENCLATURE

Acronyms

Definitions

AOA

Angle of attack

AR

Aspect Ratio

DP

Drag Peak

DPIV

Digital Particle Image Velocimetry

DPSS

Diode Pulsed Solid State

LEV

Leading Edge Vortex

MAVs

Micro Aerial Vehicles

PC

Polycarbonate

PIV

Particle Image Velocimetry

TEV	Trailing Edge Vortex
TTL	Transistor-Transistor-Logic
TV	Tip vortex
LP	Lift Peak

Symbols

Definitions

F_x	Normal force to the wing
F_y	Parallel force to the wing
L_{ref}	A reference length
U_{ref}	A reference velocity
U_{tip}	Wing-tip velocity
\bar{c}	Mean chord length

D	Drag
EI	Flexural Stiffness
f	Flapping frequency
F	Applied force
I	Second of moment of area
k	Reduced frequency
l	A physical length
L	The effective beam length
L	Lift
P_R	Power required
R	Wing length (half span length)
Re	Reynolds Number

S	Wing area (half wing)
t	Wing thickness
t	time
T	Total time each cycle
U	A linear velocity of the object
β	Wing-beat amplitude (rotating)
Φ	Wing-beat amplitude (sweeping)
ω	Mean angular velocity
ω	Velocity of vorticity
ω^*	Frequeuncy ratio
ω_n	Natural frequency

ω_{vor}	Normalized velocity of vorticity
t/T_α	Non-dimensional time for rotating wing
t/T_ϕ	Non-dimensional time for sweeping wing
t/T	Non-dimensional time
α	Angle of attack (rotating)
δ	Wing displacement
μ	Coefficient of fluid viscosity
ν	Kinematic viscosity
ρ	Fluid density
ρ_w	Wing density
ϕ	Stroke angle (sweeping)

1 INTRODUCTION

1.1 Motivation to study insect-inspired flapping air vehicles

In past decades, much research has been conducted on the flapping flight, like the concept of Leonardo da Vinci, in nature with aerodynamics study. Biological flyers, such as birds and insects, have evolved over 150 million years and are still impressive even though aeronautical technology has developed rapidly over the past 100 years. For example, the SR-71 flies at Mach 3 (~2000 mph) and covers about 32 body lengths per second while a common pigeon, one of natural flight creatures, covers to 75 body lengths per second at 50 mph speed [2]. It shows that the biological flyers are more maneuverable than conventional aerial vehicles. However, their complex flight structures or principles have been a challenge to mimic them.

Decreasing in size of aerial vehicles confronts a problem in aerodynamic force generation and flight control. The aerodynamic characteristics change considerably between the small-sized aerial vehicles and the conventional aerial vehicles due to the Reynolds number effect. Therefore, an understanding of flapping wing is a key to overcome the limitation of fixed or rotary wings in the small-sized aerial vehicles. The biological flyers need to investigate unsteady aerodynamics, flapping motions, flexible wings, as well as a rapid adaptation on different environment conditions [2]. With these biological features, high performances in free flights can be obtained.

In particular, insect flyers have encouraged many researchers to study and develop the small-sized flapping aerial vehicles for the use in reconnaissance missions in hazardous locations. In addition, all performances of insects are carried out at the wing root, and the wing weight of insects is very light, which accounts for 1% of the whole weight [3]. Insects flap their wings with large wing rotation angles that produce sufficient aerodynamic force when they fly. The flight

mechanisms of insects have been potential in Micro Aerial Vehicles (MAVs) development because of their hovering flight capacity and high maneuverability.

1.2 Insect flapping flight

The objective of this thesis is to study and develop the insect-inspired flapping MAVs with a better understanding of aerodynamic characteristics for flapping wings at low Reynolds number. Since a high speed camera was invented that record the fast moving objects like the insect's flapping wings as a photographic image on storage, insect flyers could be studied easier than before in order to develop insect-inspired flapping aerial vehicles. With the high speed camera, the various motions of insect flyers could be observed and analyzed in detail. In this chapter, the efforts in experimental and computational studies of the insect flapping flight are reviewed briefly.

1.2.1 Experimental studies in insect flapping flight

It is difficult to measure flapping motions of free flight in insects due to their high wing-beat frequency with small wing size. Flapping wings generate the unsteady aerodynamic force, so in the past some researchers tethered insects to measure flapping kinematics with the aerodynamic force and flow structures [4-7]. However, the tethered insects separated the inertial forces from the aerodynamic force. Furthermore, the flow visualizations for flapping were not clear enough and it was difficult to temporally measure the wake structures, which are related to the aerodynamic force generation in all degrees of freedom. Therefore, many researchers have developed mechanical models of insect wings with the considerations of Reynolds number in insect flapping flight.

Recently, Ellington [8] captured free-flight wing at 5000 frames per second to determine the kinematics of insects, and a high speed videography has been employed to determine the motions of their wings and bodies [9]. Using the high speed videography, researchers easily have measured the flapping kinematics each insect. Therefore, flapping kinematics have been performed

to measure aerodynamic characteristics of the flapping wing by using a dynamically scaled-up models.

1.2.2 Computational studies in insect flapping flight

Computational methods offer a different approach in solving the mechanisms in insect flapping flight. Unlike the above experimental studies using tethered insects or robotic models, the computational methods require experimental data, such as wing kinematics, to design the Computational Fluid Dynamics (CFD) models. Based on the kinematic model in hovering hawkmoth [10], Liu et al. [11] studied initially the unsteady aerodynamics by using the three-dimensional Navier-Stokes equations on a structured grid. This study confirmed the experimental results that were observed by Ellington et al. [12] in real and dynamically scaled model insect flight. Their computational results accurately predicted the complex vortex structures and the importance of the spanwise flow in stabilizing the spiral leading edge vortex (Figure 1.1). In addition, Sun and Tang [13, 14] studied the unsteady aerodynamics of a fruit fly model in 3-D Navier-stokes equations, and obtained the results roughly matching experimental results measured by Dickinson et al. [15].

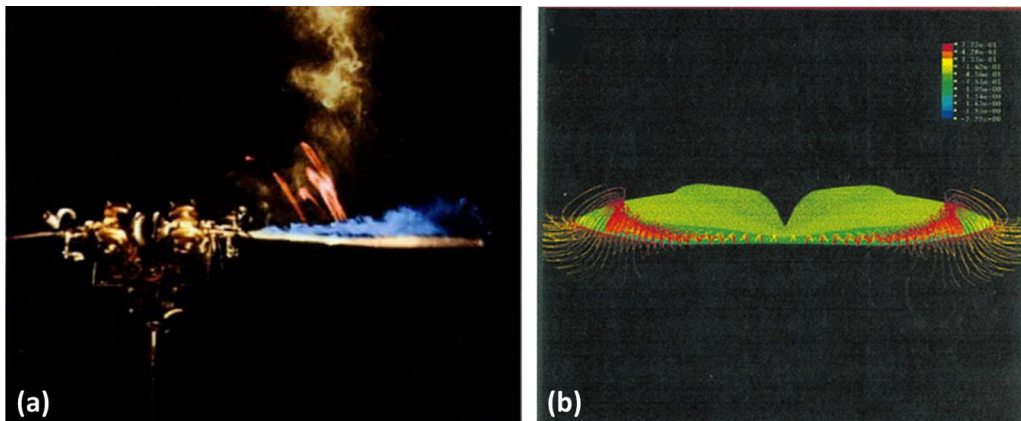


Figure 1.1 Leading edge vortex on hawkmoth wing during downstroke. (a) smoke-visualization [12] (b) computational visualization [11]

With advances in computational methods, many researchers have focused on the wing flexibility for flapping. Due to the inherent flexibility of insect wings, the aerodynamic and inertial forces for flapping insect wings can consequently induce considerable elastic deformations [16]. Fluid-Structure Interaction (FSI) problem is associated with the aerodynamics and structural dynamics of flapping wings. Experimentally, it is very difficult to solve the aero-elastic problem of flexible wing because it usually requires direct measurements of the wing deformation, the flow structures, and the aerodynamic forces [17-19]. The computational methods can approach the effects of the wing deformation on aerodynamics with relative easy. However, the computational methods still have the limits to predict the flow structures for flapping flexible wings, due to the complex unsteady mechanisms in insect flapping flight.

1.3 Unsteady mechanisms in insect flapping flight

Flapping wings show specific flow structures and their unsteady aerodynamic mechanisms such as leading edge vortex [12], delayed stall [12, 20], rotational circulation [15], and wake-capture (wing-wake interaction) [15]. Such criterion has explained how the flapping flights generate aerodynamic force such as lift and drag as shown in Figure 1.2.

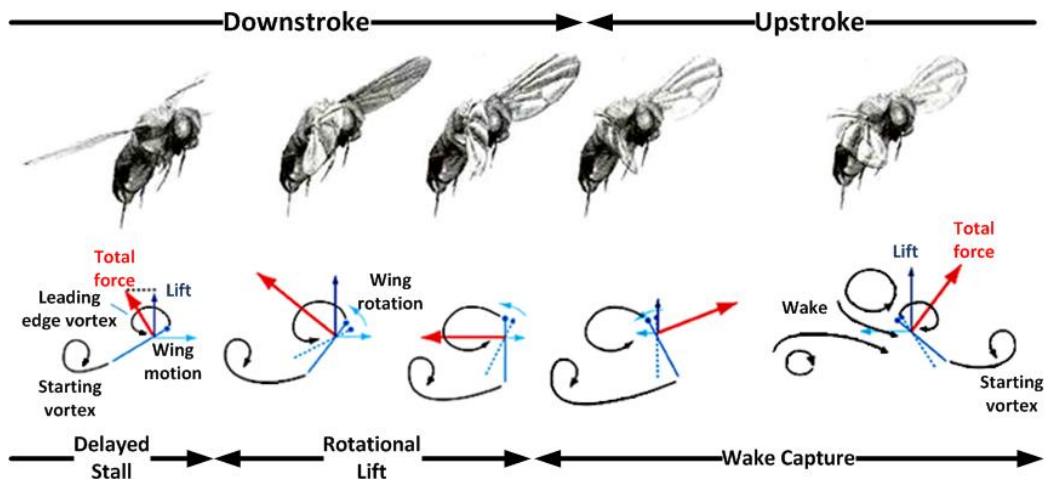


Figure 1.2 Summary of aerodynamic mechanisms in insect flapping flight, designed by Dickinson, M. H. in “Catching the Wake”, SCIENTIFIC AMERICAN™ [1]

1.3.1 Leading edge vortex and delayed stall

Flapping thin airfoils with high angle of attack present that the local viscous forces within the fluid near a leading edge are smaller than the pressure forces generated by the high fluid velocity. The flow over the wing separates at the leading edge but reattaches before reaching a trailing edge, leading to the formation of a Leading Edge Vortex (LEV). In this case, the suction force is not parallel but normal to the wing as shown in Figure 1.3. Therefore, the suction force that is adding to a normal force helps to enhance the lift and drag generation. Additionally, the resultant force in the thin wing case is perpendicular to not the ambient flow velocity but the wing.

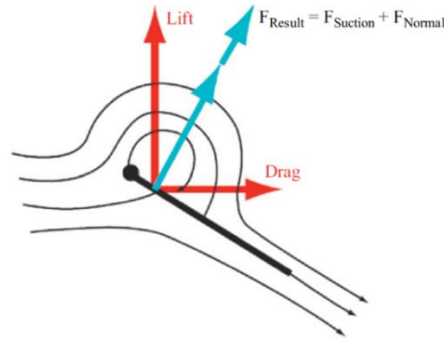


Figure 1.3 Flow around a thin airfoil [21]

Most insects flap their wings at high angle of attack, thereby the leading edge vortex plays a role in lift generation in the flights of small-sized flapping aerial vehicles [12]. For example Liu and Aono [22] presented such size effects on hovering flights like a hawkmoth, a honeybee, a fruit fly and a thrips in the range of Reynolds numbers from 10^1 to 10^4 using a biology-inspired dynamic flight simulator with an *in-house* Navier-Stokes solver. Their results showed that the LEV is a common feature for flapping wing at low Reynolds number, but the LEV characteristics to generate lift varied as different Reynolds number, reduced frequency, Strouhal number, wing flexibility, and flapping kinematics. Hawkmoth hovering showed that Trailing Edge Vortex (TEV) and Tip Vortex (TV) could contribute to generate the aerodynamic force with LEV, but lower

Reynolds numbers for honeybee and fruit fly presented that the TEV and TV became much more weaker. However, the honeybee and fruit fly could obtain the fore augmentation from the rapid rotation of the flapping wing instead of the TEV and TV. In addition, their results also showed the downstroke force to upstroke force ratio which decreased as the size or Reynolds number decreased. Furthermore, Sane [21] showed that the LEV grew in size for flapping the wing at continuously high angle of attack until the flow couldn't be reattached in 2-D linear translation. The reattached LEV prior to 'stall' generated high lift coefficients on several chord lengths, and this phenomenon was called 'delayed stall'.

Ellington et al. [12] also suggested that the delayed stall of LEV can enhance significantly lift for flapping wing through the experiments using a smoke fluid visualization around the wings, which were the hawkmoth *Manduca sexta* and a hovering large mechanical model in 3-D flapping translation. They showed that the LEV created a region of lower pressure above the wing and it enhanced the lift generation. In addition, they observed a steady spanwise flow from the wing and this spanwise flow was entrained by the leading edge vortex to spiral towards the wing tip. Through transferring the momentum in the spanwise direction with the momentum decrease in the chordwise direction, it caused the leading edge vortex to be smaller. The smaller leading edge vortex made the flow reattach easier and helped the reattachment be maintained for a longer time.

1.3.2 Rotational circulation

Dickinson et al. [15] have conducted the rotational force, which is caused by the rapid pitching-up rotation before reversing the wing. They measured the aerodynamic forces with a dynamically scaled-up model for flapping, and showed the large positive peaks which were observed for the rapid pitching-up rotation before the stroke reversal. The lift shows the negative peak in the delayed rotation due to the pitching-down when the wing rotated back after reversing

the stroke. They suggested that the insect could generate lift through the rotational mechanism as adjusting the timing of wing rotation. Sane and Dickinson [23] presented that the lift peak prior to the end of stroke was related to proportionally the wing angular-velocity, which the rotational coefficients depended on, based on a quasi-steady theory. Additionally, Sun and Tang [13] and Wu and Sun [24] revealed that the pitching-up rotation caused the circulation increment, which phenomena induced the lift increase. To sum up, the rotational circulation affects the lift increment for the pitching-up rotation prior to the end of stroke.

1.3.3 Wake-capture (wing-wake interaction)

Wake-capture is often observed when flapping wings show a wing-wake interaction. During reversing the wings in their translational direction, the wings face to the wake generated by the previous stroke so that the fluid flow is effective to increase the fluid velocity and the peak on aerodynamics is shown. Dickinson et al. [15] used a robotic model to operate simple translational and rotational motions for measuring the aerodynamic forces. While they found a specific feature to generate force peaks after reversing the stroke, Sun and Tang [13] suggested that the peaks might occur due to the added-mass acceleration after reversing the stroke and pointed out that the specific flow was not the wake but a downwash. After the opposed conclusions between those above, Birch and Dickinson [25] examined the wing-wake interaction in detail through 2-D Digital Particle Image Velocimetry (DPIV) studies to visualize the flow around the flapping wing, which was a dynamically scaled robot. They showed that the developed- and shed-vortices for each stroke had a major effect to generate the forces during flapping wings.

Recently, some researchers [26, 27] studied a fundamental approach numerically and experimentally to present the wing-wake interaction on aerodynamic forces generation on a 2-D flapping wing. Lua et al. [27] proposed two kinds of wing-wake interaction. First, the lift was

related to the induced velocity of a pair of counter-rotating wake vortices on the reverse stroke. Second, it was associated with the vortex suction effect for the wing encountered by one vortex, and the suction effect caused the net force on the wing to decrease momentarily. Han et al. [28] presented that trailing edge vortex (TEV) for wing reversal affects significantly the characteristics of the wing-wake interaction. These results suggested that the wing-wake interaction could not always affect to enhance the lift and sometimes reduce the lift. Therefore, the wing-wake interaction is still important to study and develop the insect-inspired flapping MAVs.

In fact, the wing-wake interaction is very complicated because this interaction is essentially an inter-related phenomenon between the wake generated by the previous stroke and the wing motion in the next stroke. In conventional aerodynamics, the wake can be handled as an important element of the fully unsteady aerodynamic model. Although Theodorsen [29] presented a powerful theory written in terms of Bessel functions to solve two-dimensional unsteady aerodynamics as well as the flutter, it requires not only a simplification of the wing motion and an ability to keep the traces of the shed wake, but also a relatively complicated calculation. In addition, Sane and Dickinson [23] already showed that the wing-wake interaction was highly sensitive to the function of the wing kinematics. This implies that the wing kinematics, including the rotational and the translational dynamics, have to be synthetically contemplated with the flow structures in order to understand the lift augmentation that occurs as a result of the wing-wake interaction. Further research by elucidated that the wing-wake interaction was highly sensitive to the wing kinematics and flow structures.

1.4 Wing flexibility in insect flapping flight

Insects have various flexible wing structures which are very complex to model because their wings are generally made by thin membrane with veins. The majority of prior investigations

simplified the wing structural models to assess the benefit of wing flexibilities in force generation due to the complexity on the nonlinear fluid flow. Zhao et al. [30] studied the chordwise flexibility effects with 16 different wings, which were made of polyester, polycarbonate, polyethylene and Mylar to obtain variable stiffness values. To ignore the spanwise flexibility, they attached the wing model with the rigid carbon fiber leading edge. The results from the experiments showed that the overall aerodynamic performance of flapping wings deteriorated as they became more flexible and the magnitude of force generation could be controlled by modulating the trailing edge flexibility. It shows that the wing structures as well as the chordwise flexibility are important factors to develop the insect-inspired flapping MAVs. Bi and Cai [31] also presented that the highest spanwise flexibility is not a good choice on the thrust generation and propulsion efficiency through the aerodynamic experiment in water tank.

In the experimental results of Hu et al. [32], various flexible wing structures were examined to evaluate their implications on flapping wing aerodynamics, and the research showed that the flexible membrane wings were better than rigid wing for high-speed soaring flight or at relatively high angle of attack. These experiments showed the importance to select the proper wing flexibility of the membrane skins for achieving improved aerodynamic performances in soaring and flapping flight. Additionally, other researchers [33-35] demonstrated that the maximum propulsive force was generated when a flapping frequency was lower than the natural frequency of the flapping wing. Zhang et al. [33] concluded that a flat plate would generate a thrust to move forward if a flapping motion frequency was lower than the natural frequency of the plate via the lattice Boltzmann method. Ramanarivo et al. [34] also presented that the maximum thrust was obtained at the frequency ratio, between a flapping motion frequency and a natural frequency, of

approximately 0.7. Furthermore, Vanella et al. [36] described that the best aerodynamic performance was realized at the frequency ratio of 1/3 using numerical methods.

With above efforts to construct the relations between aerodynamics and wing flexibility, some researchers [30, 37, 38] outlined the advantages and disadvantages, as well as an importance of flexible flapping wing. Hamamoto et al. [38] presented that a very thin dragonfly wing could not take the wing shape, thereby losing the aerodynamic force. Lua et al. [39] took the finding from Hamamoto et al. [38] in an endeavor to answer the relationship between the wing flexibility and aerodynamic force generation through aerodynamic experiments. Their results demonstrated that wings with a specific stiffness could generate mean lift coefficient similar to that of a rigid wing in a hawkmoth motion, but less than that of a rigid wing in a sinusoidal flapping motion. However, the appropriate wing flexibility for insect-inspired flapping MAVs and the difference of flow structures between the rigid and flexible wings that affects the aerodynamic force deterioration have yet to be elucidated.

1.5 Hovering flight

Some insects, such as fruit fly and hawkmoth, are capable of hovering flight, and the insects have two translational phases, upstroke and downstroke, and two rotational phases, pronation and

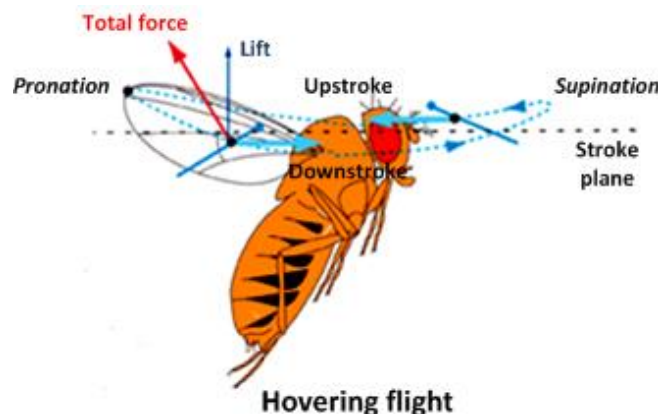


Figure 1.4 Hovering flight of fruit fly [1]

supination [1]. Figure 1.4 shows the sample hovering flight of fruit fly. Downstroke and upstroke describe the dorsal to ventral motion and the ventral to dorsal motion of the wing, respectively. Supination is the rapid transition of downstroke-to-upstroke and pronation is the rapid transition of upstroke-to-downstroke.

1.6 Experiment Facility

The aerodynamics experiments in this thesis have been conducted by ongoing collaboration between Ryerson University and Korea Aerospace University. Due to the lack of equipment for unsteady aerodynamics experiment in Ryerson University, the experiments to study the flapping flights were performed at Dr. Jo Won Chang's Applied Aerodynamic Laboratory in Korea Aerospace University. Figure 1.5 shows Dr. Chang's laboratory in Korea Aerospace University, and his laboratory has carried out the experimental researches for Micro/Nano Aerial Vehicles and ornithopter. There is equipment to measure the flow fields on aerodynamics: suction-type subsonic wind tunnel (size: 10.1 m × 2.0 m × 2.0 m), blow-type wind tunnel (size: 7 m × 2.0 m × 2.0 m), water tank (size: 3.5 m × 1.0 m × 1.1 m), vacuum chamber, pressure transducer, Particle Image



Figure 1.5 Dr. Chang's laboratory in Korea Aerospace University

Velocimetry (PIV) systems including a high speed camera and a laser, Dantec StreamLine (R) system, force data acquisition systems, etc.

1.7 Aims and objectives in present study

The main objective of this thesis is to investigate the experimental aerodynamics on flapping flexible hawkmoth-like wings in hovering flight. Based on above studies of insect flight, it is clear that a better understanding of the unsteady aerodynamic mechanisms is important for the development of MAV-sized flapping aerial vehicles. Hawkmoth-like wing models are derived from *Manduca sexta*, and the wing thickness is chosen as design variables to simplify the comparison between various wing flexibilities. The wing models with spanwise length of 200 mm and an aspect ratio of 6.18, are constrained to a symmetrical motion and sinusoidal flapping motion with sweeping and rotating amplitude of 120° and 90° at Reynolds number (Re) of 10,744 in water tank with size of 3.5 m × 1.0 m × 1.1 m. Aerodynamic force and flow structures for flapping the wing models are measured by a six-axis force/torque sensor and a high speed camera with a laser using Digital Particle Image Velocimetry (DPIV) method.

2 EXPERIMENTAL SETUP AND PROCEDURE

Many fluid-dynamic coefficients such as the lift and drag coefficients are related to the Reynolds number. The Reynolds number (Re) in this thesis can be defined as the following:

$$\text{Re} = \frac{\text{Inertial Force}}{\text{Viscous Force}} = \frac{\rho U^2 l^2}{\mu U l} = \frac{U_{ref} L_{ref}}{\nu} = \frac{(\omega R) \bar{c}}{\nu} \quad (1)$$

where U is the linear velocity of the object, U_{ref} is a reference velocity, l is the physical length, L_{ref} is a reference length, μ is the coefficient of fluid viscosity, ν is the kinematic viscosity, and $\nu = \frac{\mu}{\rho}$, ρ is the fluid density. U_{ref} changes to the mean wingtip velocity (ωR); R is the wing length (half span length), ω is the mean angular velocity of the wing, and \bar{c} is the mean chord length, $\bar{c} = S/R$.

The mean angular velocity of the wing is related to the wing-beat amplitude and the flapping frequency:

$$\omega = 2\Phi f \quad (2)$$

where Φ is the wing-beat amplitude in radians, and f is the flapping frequency

The ratio between the forward velocity and the flapping velocity is important for aerodynamic performance, and in hovering flight this reduced frequency can be obtained by the following equation:

$$k = \frac{\pi f \bar{c}}{U_{ref}} = \frac{\pi f \bar{c}}{\omega R} \quad (3)$$

In this experiment, the wing-beat amplitude, Φ , is 120° and a wingbeat frequency, f , is 0.16 Hz. The water temperature, which affects water density, ρ , and viscosity, ν , is $16.3 \pm 0.53^\circ\text{C}$. The mean chord length, \bar{c} , was 0.0647 m. Based on these data, the reduced frequency is 0.24 and the calculated average value of Reynolds numbers is 10,744 in this thesis.

2.1 Wing models

Hawkmoth-like wing model, which is derived from a *Manduca sexta*, is selected in this experiment as shown in Figure 2.1 (a). The hawkmoth-like wing has been studied for several years in order to improve the development of insect-inspired flapping MAVs due to its well-hovering flight with relatively heavy weight in comparison with other insects. Figure 2.1 (b) shows that a wing geometry of Usherwood and Ellington [40] is redrawn as the target model in this experiment. The wing models have a half-span length, R , of 200 mm, a mean chord length, \bar{c} , of 64.7 mm, a wing area (S), 0.01294 m^2 , and an Aspect Ratio, AR , of 6.187. Due to the experimental environment corresponding to the environment of flapping insects in nature, a wing-beat frequency is much lower than that of the real hawkmoth to maintain the range of Reynolds numbers. Therefore, the Reynolds number, which is calculated with function of the mean angular velocity, is 10,744 in this experiment by using above equation (1). For the distributions of wing flexibility, the wing models are made of only pristine Polycarbonate (PC) sheet, and the wing thickness (t) is a design variable in the present study. Case 1 is a rigid wing with thickness of 3 mm, and case 2 to 8 are flexible wings with thickness of 2, 1, 0.8, 0.5, 0.35, 0.2, and 0.1 mm.

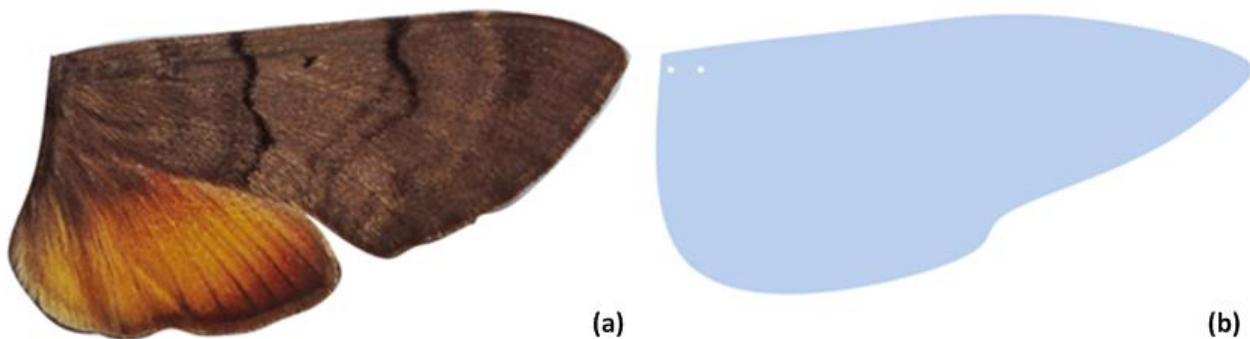


Figure 2.1(a) Real hawkmoth wing (b) Hawkmoth-like wing model used in current experiment

In current study, flexural stiffness (EI) values of wing models are calculated by the method which was described by Combes and Daniel [41]. They did not know the Young's modulus (E) as

well as the second moment of area (I) each wing because their wing models were various real insects wings. For this reason, they obtained the flexural stiffness by measuring insect wing displacement in response to an applied force at approximately 70 % of wing span and chord, and used the beam theory to calculate the bending stiffness in both directions using the following equation:

$$EI = \frac{FL^3}{3\delta} \quad (4)$$

where F is the applied force, L is the effective beam length (chord or half-span length), and δ is the wing displacement.

By comparing to the calculated flexural stiffness in both directions, Combes and Daniel [41] found that the spanwise flexural stiffness was one to two orders of magnitude that is greater than the chordwise flexural stiffness. Mountcastle and Daniel [42] also borrowed above method to calculate a spanwise flexural stiffness of real *Manduca sexta*'s wing, and reached the conclusion that the flexural stiffness for the real insect wing has the range of 10^{-6} to 10^{-5} Nm^2 in common with Combes and Daniel [41]. In addition, Zhao et al. [43] and Lua et al. [39] designed their wing models which were made of various materials and had different wing-thicknesses. Zhao et al. [43] had the insect-inspired flexible wings attached with spanwise rigid carbon fibre vein, thereby they characterized the flexural stiffness in the direction of wing chord using the equation (5). In the study of Lua et al. [39], different flexibilities of the wing models were performed by different materials and fabricated real hawkmoth-like veins. They measured the spanwise flexural stiffness of each wing using the above method. However, above experimental method to obtain the flexural stiffness is not suitable in this experiment due to the large wing models relatively compared to the real flapping insects. Additionally, case 6 to 8 were too bending to measure the flexural stiffness using above experimental method. Furthermore, the wing models in the current study are made of

Polycarbonate (PC) sheets, which sheets of different thickness were cut by using a computerized numerically controlled (CNC) machine tool, and there was no shape-deformation in this process. Young's modulus (E) of the pristine PC sheets is 2.5 GPa so the method described in Combes and Daniel [41] is not needed in this study. For calculating the spanwise flexural stiffness (EI), the second moment of area (I) is required only in this experiment. They calculated the second of moment of area from the flexural stiffness for each half-span length (R) with the following equation in Gordon [44]:

$$I = \frac{Rt^3}{12} \quad (5)$$

In order to present the relationship between the wing and aerodynamic force, non-dimensional stiffness (EI_{non}) is calculated by the following equation [18, 39, 45]:

$$EI_{non} = \frac{EI}{\rho_f U_{ref}^2 \bar{c}^4} \quad (6)$$

where ρ_f is the density in fluid; a water density in current study

As mentioned earlier, the flapping frequency is lower than the natural frequency of the wing model to obtain maximum thrust and power efficiency. In the current experiment, the natural frequencies in all cases are larger than the flapping frequency, 0.16 Hz as shown in Table 1. The natural frequency (ω_n) is calculated by following the first mode frequency equation, which assumes a cantilever beam hypothesis:

$$\omega_n = \frac{3.5156}{2\pi L^2} \sqrt{\frac{EI}{\rho_w S}} \quad (7)$$

where ρ_w is the density of wing model

Finally, Table 1 shows the non-dimensional flexural stiffness and the frequency ratios (ω^*), which are used for comparing the effect of flexibility among different wing models that are used in this experiment. Sunada et al. [46] measured the natural frequencies of vibration in air with four different dragonfly wings and had the frequency ratio in the range of 0.3-0.46. Ramanarivo et al. [34] also described that the maximum thrust was obtained at the frequency ratio, between a flapping motion frequency and a natural frequency, of approximately 0.7. Vanella et al. [36] described that the best aerodynamic performance was realized at the frequency ratio of 1/3 using numerical methods. In the current experiment, the wing models have the frequency ratio in the range of 0.05-1.73. The frequency ratio is given by Yin and Luo [47] and Tian et al. [48] with following equation:

$$\omega^* = \frac{2\pi f}{\omega_n} \quad (8)$$

Table 1 Wing data in the present experiment

Case	Thickness (mm)	I (m ⁴)	EI (Nm ²)	EI_{non}	ω_n	ω^*
1	3	4.5×10^{-10}	1.125	1892.095	17.412	0.05773
2	2	1.333×10^{-10}	0.333	560.994	11.608	0.0866
3	1	1.667×10^{-11}	0.0417	70.124	5.804	0.1732
4	0.8	8.533×10^{-12}	0.0213	35.876	4.643	0.2165
5	0.5	2.083×10^{-12}	0.00521	8.759	2.902	0.3464
6	0.35	7.146×10^{-13}	0.00178	3.005	2.031	0.4948
7	0.2	1.333×10^{-13}	0.000333	0.5607	1.1608	0.866
8	0.1	1.667×10^{-14}	4.167×10^{-5}	0.07009	0.5804	1.732

2.2 Water tank and experimental motion model

As earlier stated, the experiments in this thesis were performed at Dr. Chang's laboratory in Korea Aerospace University. The 3-D flapping wing mechanism is shown in Figure 2.2, and wing models moved as the motion kinematics for hovering in water tank with size of 3.5 m ×

1.0 m \times 1.1 m. The motion model for sweeping and rotating the wing is composed of two servo motors (MX-28T, ROBOTIS Inc.), which are equipped at upper and lower sections of a dual-connect frames. The upper servo motor with a horn, mounted under the upper aluminum plate, drive the sweeping motion (sweeping angle, ϕ) along the X-Y plane. The rotation motion (rotating angle, α) along the X-Z plane is also operated by the lower servo motor, which is connected with both the dual-connect frames and the aluminum pipe. Two servos are connected in parallel, and each servo has an encoder resolution of $1/4096^\circ$ for a highly precise motion control. The servo motors are able to control the position with a full 360-degree revolution, and they use the Transistor-Transistor-Logic (TTL) communication to connect with a computer based on the codes written in LabViewTM in Figure 2.3.

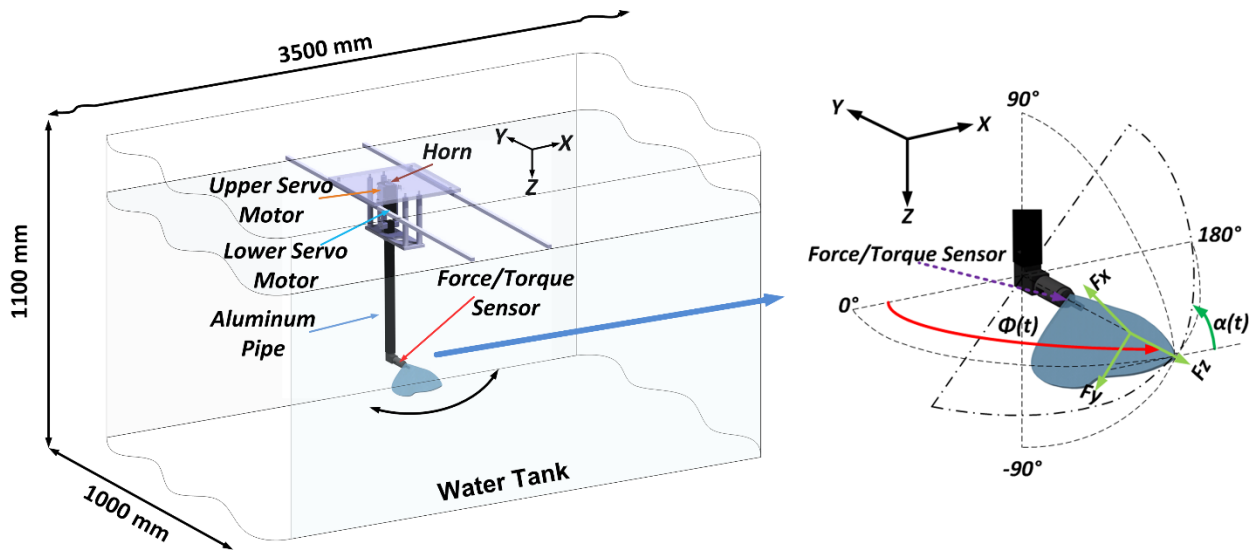


Figure 2.2 Water tank and Flapping motion coordinates in current experiment

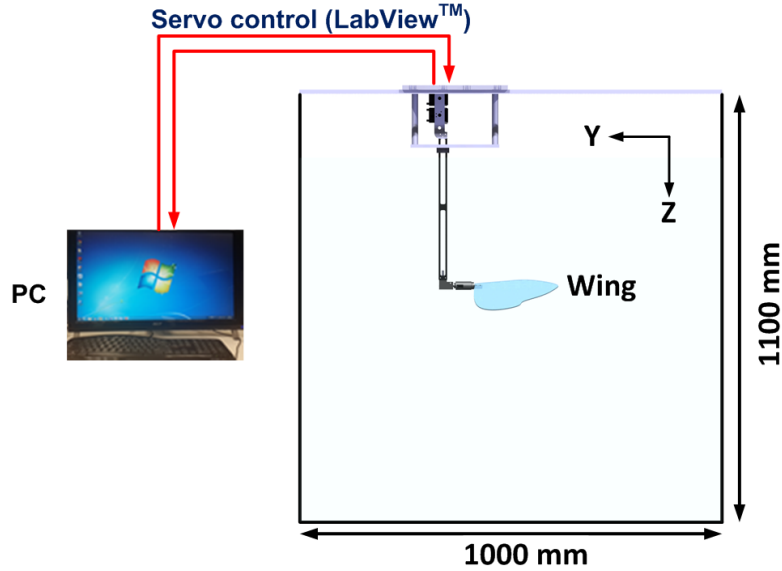


Figure 2.3 Experimental Setup: Side-view

2.3 Kinematics

Since researchers [8, 9, 49] measured the trajectories of flapping wing in hovering flights, kinematic data from their studies was available to draw the hovering motion. Ellington [8] attempted to capture free flight and hovering flight kinematics using single image high speed cine, and Willmott and Ellington [9] employed a high-speed videography to get greater light sensitivity and easier use. Fry et al. [49] also used three-dimensional infrared high-speed video to capture the wing and body kinematics of free-flying fruit flies. In addition, Dickinson et al. [15] and Sun and Tang [13] considered a similar flapping motion to show a normal hovering flight, and their studies suggested that three parts of each stroke, as shown in Figure 2.4. The wing rotates pitching-down (red arrow in Figure 2.4 downstroke 1 and upstroke 4) and accelerates on sweeping direction at the beginning of the stroke, and the wing moves at constant speed and angle of attack during the middle of stroke. Last part is the pitching-up rotation (red arrow in Figure 2.4 downstroke 3 and upstroke 6) and the deceleration on sweeping at the end of the stroke. Furthermore, Sun and Tang [14] compared their calculated results in hovering flight with previous data from Ellington [8], and

suggested that a duration of wing rotation (t/T_ϕ and t/T_α , non-dimensional rotation time along ϕ and α respectively) was able to assume reasonably 20% of period of one flapping cycle. This motion was considered in this experiment as a symmetrical flapping motion in Figure 2.5 (a).

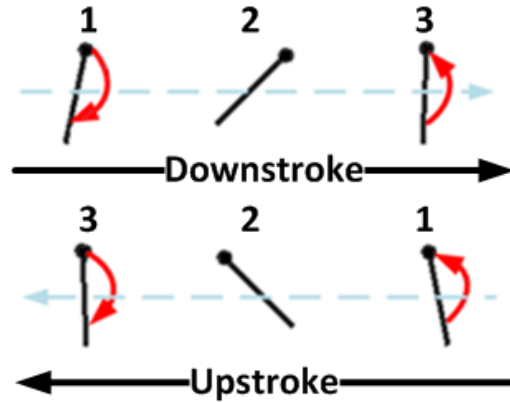


Figure 2.4 The wing motion sketches: 1. Pitching-down, 2. Constant, 3. Pitching-up, designed by Sun and Tang [13]

In present study, a sinusoidal flapping motion is also investigated for comparing the symmetrical flapping motion. Wang et al. [50] compared computational, experimental, and quasi-steady forces for hovering with sinusoidal motion along a horizontal stroke plane. Lua et al. [39] also derived sinusoidal motion on the above, called a simple harmonic motion in their paper, in order to compare with hawkmoth flapping motion. In current study, such sinusoidal flapping motion is used to compare the overall effect on aerodynamics by wing flexibility each wing. Figure 2.5 (b) presents the sinusoidal flapping motion with the peak amplitudes in sweeping motion (ϕ) and rotating motion (β) of 60° and 45° respectively. The sinusoidal flapping motion was defined by the following equations:

$$\phi(t) = \phi \cos(2\pi ft) \quad (9)$$

$$\alpha(t) = \alpha_0 + \beta \sin(2\pi ft) \quad (10)$$

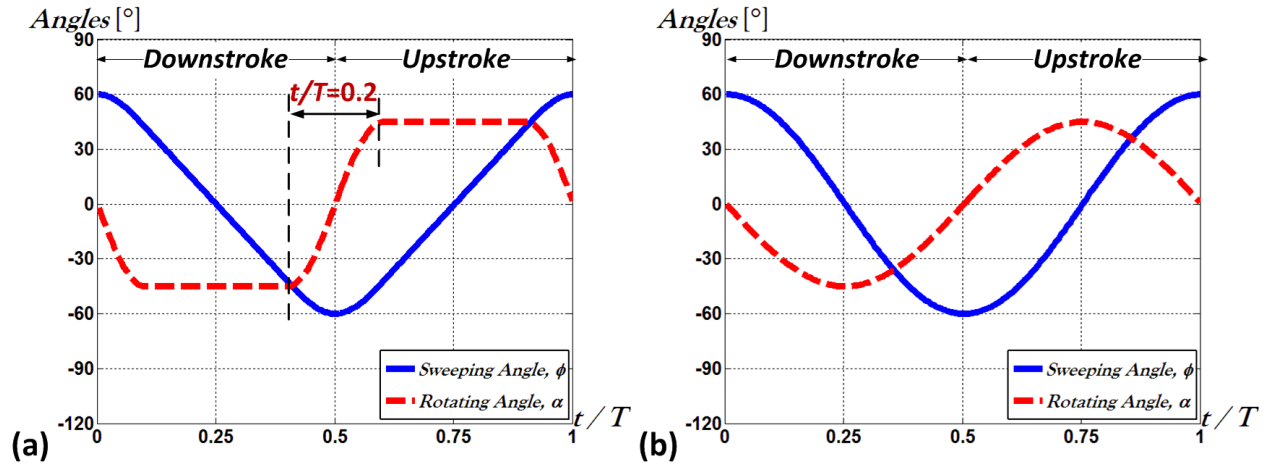


Figure 2.5 Flapping wing motions: (a) Symmetrical flapping motion (b) Sinusoidal flapping motion

2.4 Force Measurements

Figure 2.6 shows that a six-axis micro force/torque sensor (NANO 17 IP68, ATI Industrial Automation) is mounted on the wing-root side on the leading edge. The sensor has the measurable ranges of forces and moments, ± 25 N and ± 250 N · mm respectively, and it can operate under 4 m depth of water. Figure 2.6 presents the scheme of force measurements and shows how the force and moment data are measured for flapping the wing model. Six raw signals from the sensor are stored in the computer as each angular position for the flapping model. The signals of forces and moments pass through a signal conditioner and MIO-16E4 DAQ-board to save them in the computer. Each case for flapping is separated by 250 points in this experiment, and the measurements of forces and moments are repeated over 250 times to converge the ensemble averaged values. With a calibration error of 0.51%, the error of the repeated measurements obtains 1.133% using Type-A equation with the standard deviation of force data (detail calculation process in Appendices A). The value of precision errors is 2.283% in accordance with above errors. In addition, the bias errors have 0.00794 % in horizontal alignment of the model and 0.00152 % in

DAQ systems. Considering the precision errors, the force measurement uncertainty at 95% confidence is 3.196% in this experiment.

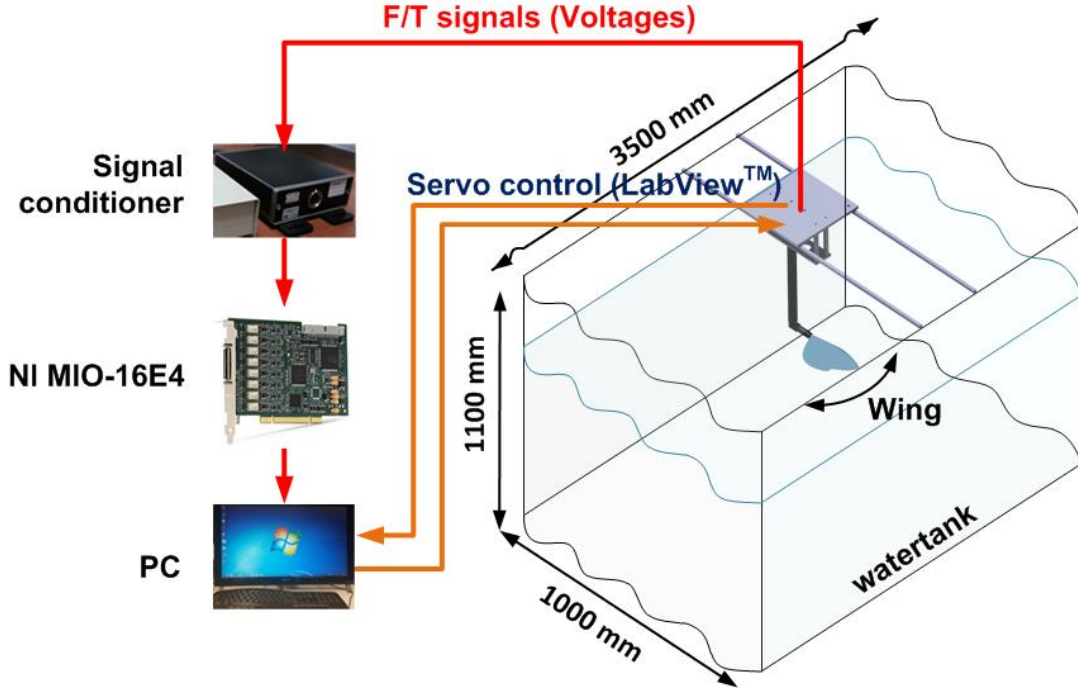


Figure 2.6 Scheme of Force measurement

The sketch of force vectors to calculate lift and drag for flapping wing is shown in Figure 2.7. The lift and drag are extracted by normal and parallel forces to the wing, F_x and F_y , and they are given by

$$L = F_x \cos(\alpha) - F_y \sin(\alpha) \quad (11)$$

$$D = \pm[F_x \sin(\alpha) + F_y \cos(\alpha)] \quad (12)$$

Furthermore, lift and drag coefficients are calculated by following equations:

$$C_L = L / \left(\frac{1}{2} \rho U_{ref}^2 S \right) \quad (13)$$

$$C_D = D / \left(\frac{1}{2} \rho U_{ref}^2 S \right) \quad (14)$$

where U_{ref} is the wing tip velocity in hovering flight

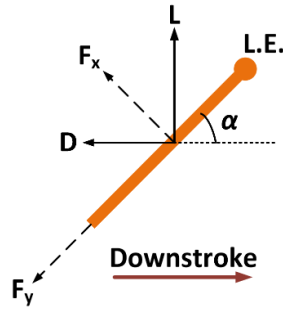


Figure 2.7 Definition of force vectors on the wing

2.5 Digital Particle Image Velocimetry (DPIV)

Digital Particle Image Velocimetry (DPIV) is an optical technique to measure the velocity of very small sized speeding-particles in the order of 10 to 100 micrometers with a laser and a speed camera. Each wing is dynamically actuated with a wing-beat frequency in water tank, and DPIV measurements are employed to study the chordwise cross-section of fluid flows around the flapping wing as shown in Figure 2.8. Shyy and Liu [51] suggested to determine the chordwise cross-section of $0.6R$ (where R is a wing length) for ignoring three-dimensional effects such as the wingtip vortex, and Birch and Dickinson [52] chose $0.65R$ as their measurement point because this point showed that the leading edge vortex was still attached and exhibited near-maximal spanwise vorticity. In current study, $0.5R$ chordwise cross-section is selected for ignoring three-dimensional effects, such as the wingtip vortex.

The DPIV system consists of a high speed camera (FASTCAM SA3, Photron) and 1.5W Diode Pulsed Solid State (DPSS) laser with a standard lens (AF-S NIKKOR 50 mm F1.8G, Nikon). For the highly precise time-resolved measurements, the computer transmits a trigger pulse to the high speed camera with temporally running codes for the wing motions. The high speed camera can take 1,040 pictures totally of $1,024 \times 1,024$ pixels, and sequential 50 images at 125 frames/s are captured whenever the camera received the trigger pulse. In total, 40 pairs of pictures are used

to average the extracted flow vector field. To convert the captured images to the vector field image, PIVlab 1.32, which is a toolbox in MATABL, is used in this thesis. The program is operated in 32×32 pixel interrogation with 50 % overlap on each image, and thereby the DPIV results have 64×64 resolution.

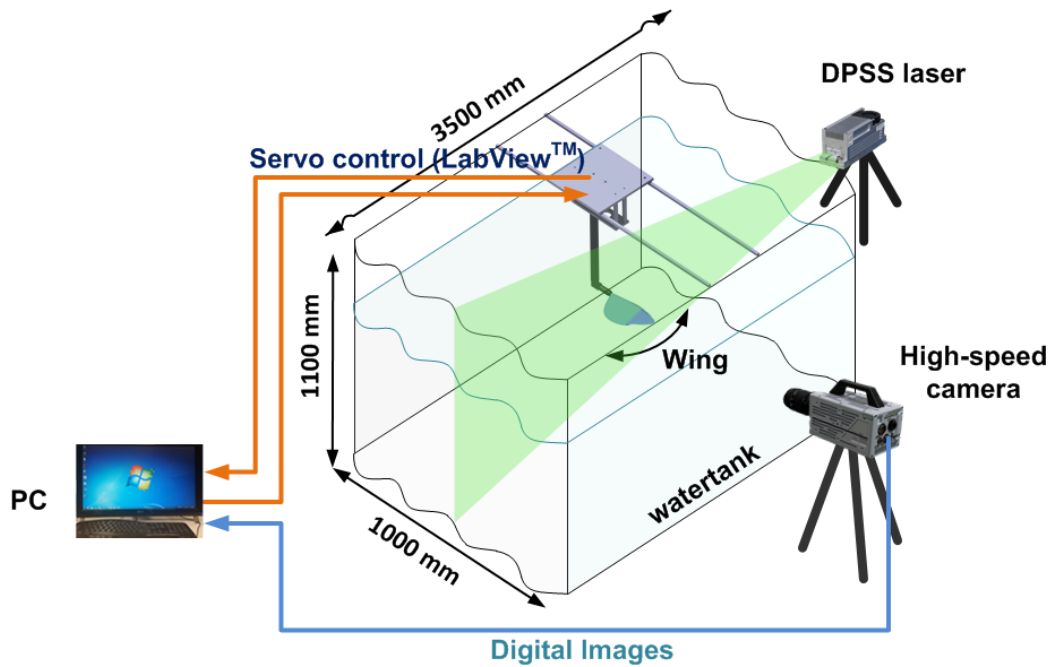


Figure 2.8 Scheme of Digital Particle Image Velocimetry (DPIV) system

3 RESULTS AND DISCUSSION

3.1 Rigid wing

3.1.1 Symmetrical flapping motion

Figure 3.1 shows the schematic trajectory of symmetrical flapping motion in this experiment. The symmetrical flapping motion presents that the wing is rotated in short time at the start and end of each stroke. As stated previously, the duration of wing rotation is able to assume 20% of period of one flapping cycle ($t/T_\phi = 0.2$ and $t/T_\alpha = 0.2$), as presented in Figure 2.5 (a). To analyze the aerodynamic characteristics in the symmetrical flapping motion, the rigid wing model in case 1 and previous studies [13, 14, 28] are firstly discussed as shown in Figure 3.2.

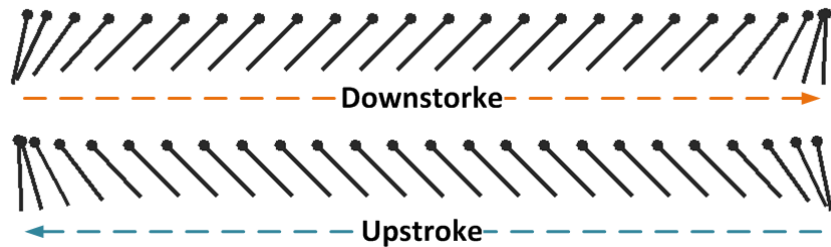


Figure 3.1 Trajectories of symmetrical flapping motion

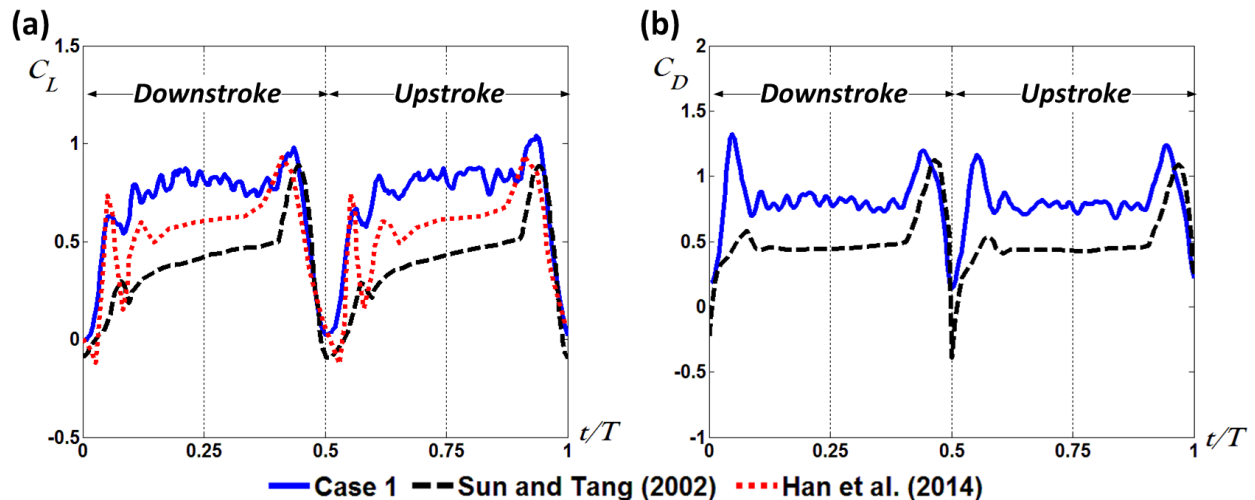


Figure 3.2 Lift and drag coefficients distributions of rigid cases in a symmetrical flapping motion

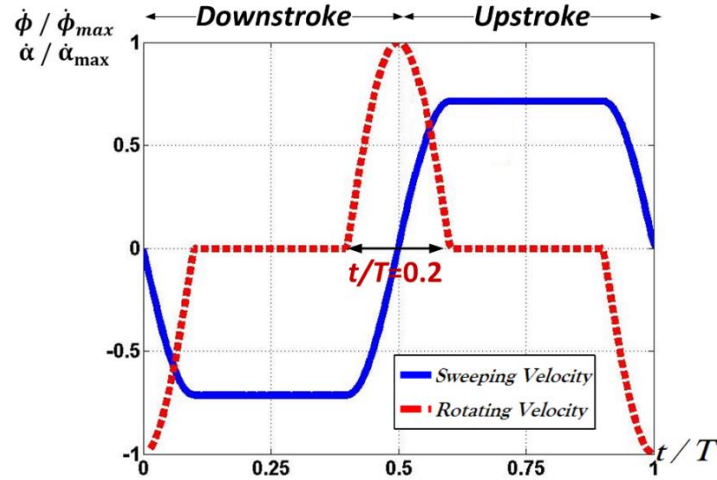


Figure 3.3 Normalized sweeping and rotating velocities each cycle in a symmetrical flapping motion

Figure 3.2 presents the results of lift and drag coefficients in case 1 (rigid wing with thickness of 3 mm in this experiment), Sun and Tang [14], and Han et al. [28]. There are three peaks in the lift coefficient and two peaks in the drag coefficient each data. Dickinson et al. [15] and Sun and Tang [14] presented the first peak and re-generation of lift before reaching third peak. The first and second peaks are signified by the enhanced force mechanisms such as the wing-wake interaction. Han et al. [28] also explained that the rotating time, t/T_α , affects the peak point and the effective range of the rotational forces through their experimental data. Comparing the results of different rotating times, each peak developed from the start of the wing rotation and converged gradually as the wing was nearing the stroke reversal.

Furthermore, Sun and Tang [14] (black dash-line) has a small first peak in the distributions of lift and drag coefficient after the wing reversal in comparison with other results. Their wing model, derived from a *Drosophila virilis*, was constrained to the symmetrical flapping motion with sweeping angle of 150° and rotating angle of 103° for $t/T_\alpha = 0.19$. The reason why their first peak is very small is because the wing flapped with the large sweeping angle. Wang et al. [50] and

Lua et al. [39] presented that the high first peak in the aerodynamic forces of the wing was caused by its small sweeping amplitude. When the sweeping amplitude is small, the wing stops and reverses in the wake at a high sweeping velocity. Thus, it causes the large peak in the aerodynamic force after the wing reversal. For this reason, Sun and Tang [14] had very small peak right after the wing reversal.

In Han et al. [28] (red dot-line), their wing had similar dimensions of the current hawkmoth-like wing. The amplitudes of sweeping and rotating motions were 120° and 90° respectively, and the periods of sweeping or rotating, t/T_ϕ or t/T_α , were 0.12, 0.24, and 0.5 each period. As shown in Figure 3.2, the lift coefficient in the current rigid case is compared with one of their results, t/T_ϕ or $t/T_\alpha = 0.24$. They found that the wing-wake interaction was impacted by the rotational profiles rather than the translational profiles (sweeping angle). They concluded that the distinction of the peak levels each rotating period explained that the wing-wake interaction was more strongly influenced by the rotational motion of the wing with their flow visualizations.

Figure 3.4 re-presents the time-resolved lift and drag coefficients of case 1 in above Figure 3.2. The lift coefficient shows dual peaks (LP1 and LP2) after the wing reversal and last peak (LP3) before the wing reversal. The dual peaks can be explained by the wing-wake interaction with the generation of leading edge vortex, and last peak (LP3) can be explained by the pitching-up motion (rotational force). In the drag coefficient, two peaks after and before the wing reversal (DP1 and DP2) are observed. DP1 is caused by the wing velocity increase with high angle of attack and the wing-wake interaction, and DP2 also occurs due to the pitching-up motion. To explain such peaks in the lift and drag coefficients each cycle, the current study provides supportive reasons based on the DPIV results to capture at near each peak-time.

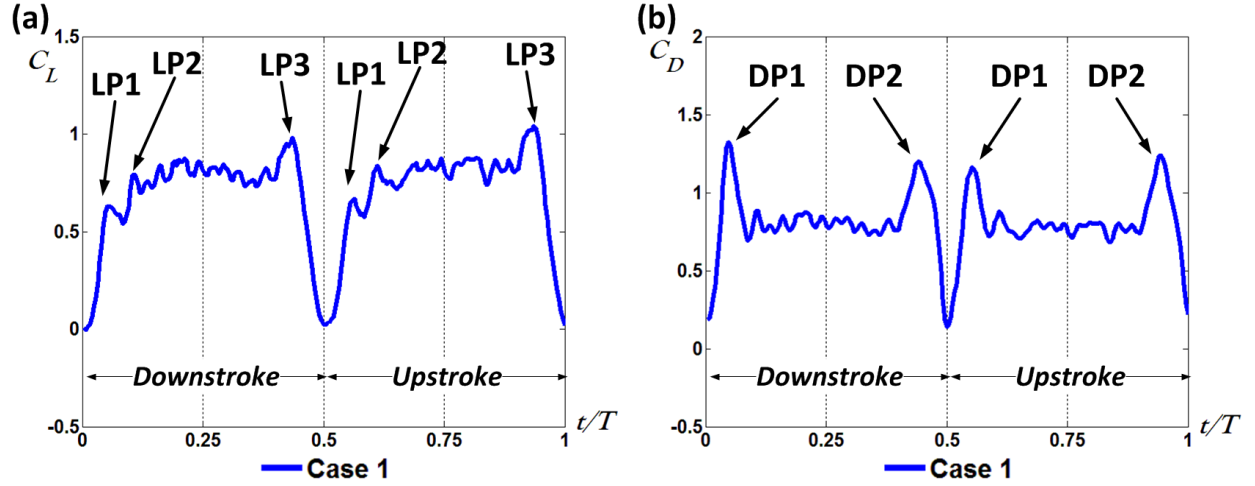


Figure 3.4 Lift and drag coefficient distributions of case 1 in a symmetrical flapping motion

Figure 3.5 shows the DPIV results of case 1 at 0.5R chordwise cross-section in a symmetrical flapping motion, and it shows the velocity vector field and the vorticity distributions at $t/T = 0.05, 0.1, 0.25, 0.45,$ and 0.55 . The vorticity, ω_{vor} , is normalized by the following equation:

$$\omega_{\text{vor}} = \frac{\omega \bar{c}}{U_{\text{ref}}} \quad (15)$$

where the normalized vorticity (ω_{vor}) has the range between -5.26 and 5.26 in the symmetrical and sinusoidal flapping motions.

Figure 3.5 (a) presents that LEV 1, generated by previous stroke, is going down under the wing and LEV 2 is growing up at the leading edge after the wing reversal. With the LEV 2 generation, the first steep peak is caused by the wake which induces the rapid flow between LEV 1 and TEV 1. Because of the wing reversal in a short time, TEV 1, generated by previous stroke, is close to the wing. Therefore, the vortices induce the velocity increase toward the wing and the induced velocity arises the lift augmentation (LP1) right after the wing reversal. This is called ‘wing-wake interaction’. After obtaining the effect of wing-wake interaction, the lift increases continuously until the sweeping velocity is constant (LP2 at $t/T = 0.1$). The last peak (LP3) is due

to the dominant effect of the pitching-up motion of the wing over the wing slowing down [39]. As shown in Figure 3.3, the constant sweeping velocity decreases again after $t/T = 0.4$ so the aerodynamic force is also expected to decrease by following the sweeping motion. However, the lift coefficient increases with the velocity decrease, and then decreases steeply. As stated previously, some researchers [13, 23, 24] found the lift increase before the wing reversal. They revealed that the pitching-up rotation caused the circulation increment, which phenomena induced the lift increase. Figure 3.5 (d) also presents no specific flow structure to cause the lift increase so the lift augmentation before the end of stroke can be expected to occur due to the rotational force.

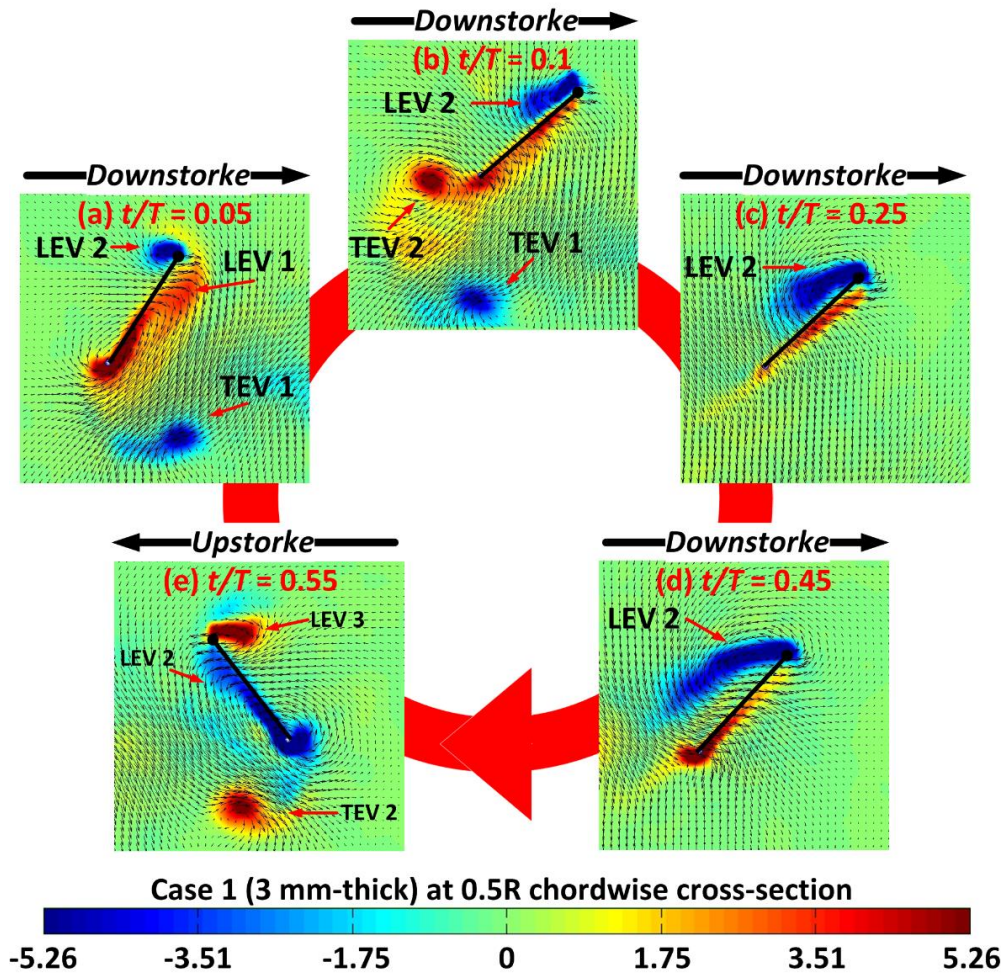


Figure 3.5 Time-resolved flow structures of case 1 at 0.5R chordwise cross-section in a symmetrical flapping motion: (a) $t/T = 0.056$, (b) $t/T = 0.1$, (c) $t/T = 0.25$, (d) $t/T = 0.45$, (e) $t/T = 0.55$

In the drag coefficient, two peaks are occurred respectively after the start of stroke and before the end of stroke. Because the first peak (DP1) in drag coefficient can occur from the sweeping velocity increase with high angle of attack, it is unclear whether the first steep peak is caused by the wing-wake interaction or not. In a sinusoidal flapping motion, drag coefficient has a steep peak after the wing reversal even if there is no wing-wake interaction; it will be discussed in detail next chapter. However, the wing-wake interaction still has an effect on the steep increase of drag in the symmetrical flapping motion. The drag generation coincides with the lift generation for flapping, thereby the flapping wing obtains more drag force due to the wing-wake interaction. Furthermore, the pitching-up motion before the end of stroke causes the last peak (DP2) in drag coefficient, like the last peak in the lift coefficient.

3.1.2 Sinusoidal flapping motion

Figure 3.6 presents the schematic trajectory of simple harmonic flapping motion in this experiment. As shown in Figure 2.5 (b), the wing rotates continuously until the peak point at the middle of stroke, and then reverts back to the original position at the end of stroke. In line with previous chapter, the rigid wing model is firstly investigated for studying the general features, such as aerodynamic characteristics and flow structures, in a sinusoidal flapping motion.

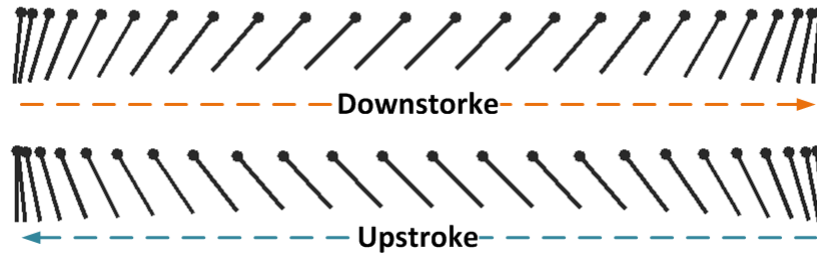


Figure 3.6 Trajectories of sinusoidal flapping motion

Figure 3.7 shows the distributions of lift and drag coefficients for the rigid wing with established studies [39, 50]. The rigid wing in case 1 (blue, solid-line) shows two peaks around the middle of stroke in the lift coefficient distribution, even though the lift coefficient generally reflects the sinusoidal flapping motion. Before reaching the first peak around $t/T = 0.5$, the lift increase is related to the velocity increase of flapping wing and the LEV 2 generation (shown in Figure 3.10). Figure 3.8 presents sweeping and rotating velocities, which are normalized by each maximum velocity. The sweeping velocity (blue, solid-line) increases while the rotating velocity (red, dash-line) decreases from the start of each stroke. With the increase of sweeping velocity after wing reversal, some studies [12, 25, 27] showed that the growing LEV 2 causes the lift generation prior to decreasing the sweeping velocity again. However, Wang et al. [50] presented a steep peak of lift coefficient right after reversing the wing as shown in Figure 3.7 dash-line. By virtue of their result, they indicated the relation between the magnitude of the steep peak in lift

coefficient and that of sweeping amplitude (ϕ). Lua et al. [39] also supported that the steep peak was reduced as the sweeping amplitude was increased. The current study has the sweeping amplitude of 120° so no steep peak right after reversing the wing is measured in the lift coefficient.

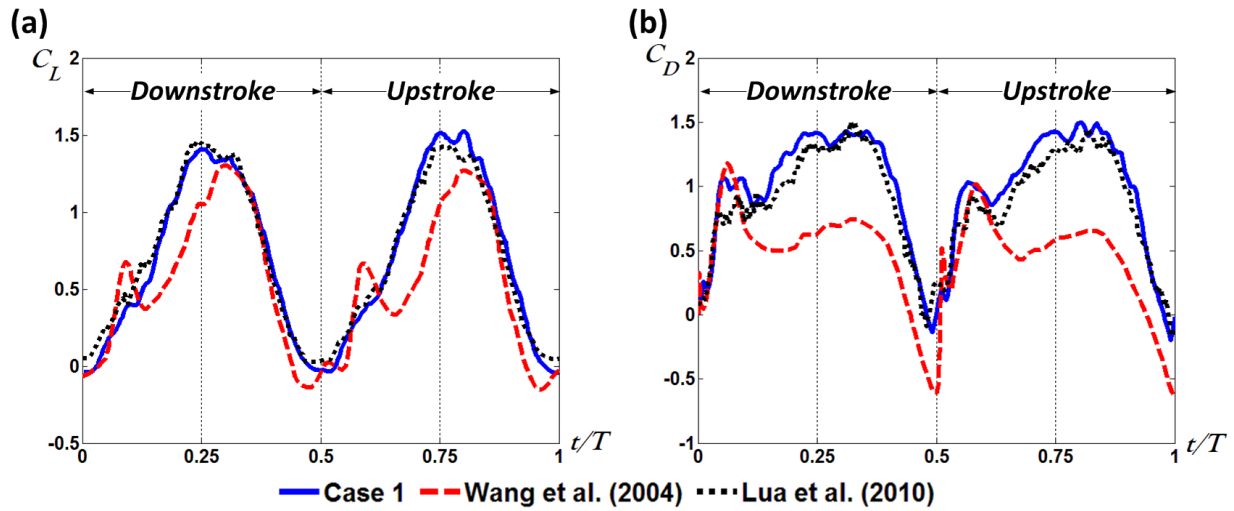


Figure 3.7 Lift and drag coefficient distributions of rigid cases in a sinusoidal flapping motion

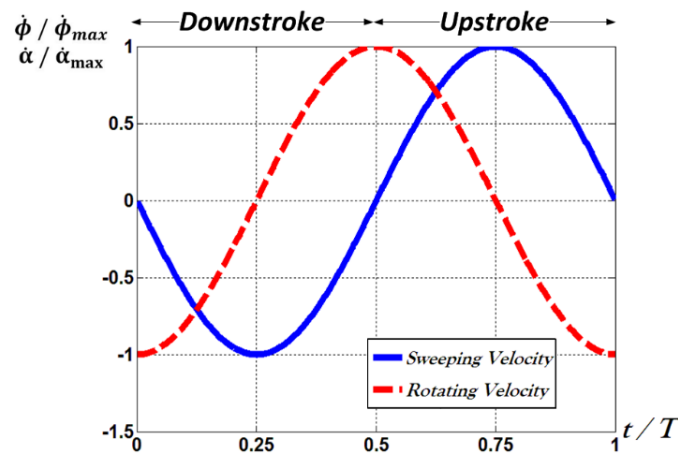


Figure 3.8 Normalized sweeping and rotating velocities each cycle in a sinusoidal flapping motion

After the maximum sweeping velocity (blue, solid-line) reaches at the middle of stroke in Figure 3.8, the wing model slows down and the lift correspondingly diminishes. However, the lift increases again by presenting the second peak as shown in Figure 3.9 (a) LP2. With reference to

findings by Lua et al. [39], this increase can be explained that a pitching-up motion of the wing seems to have the dominant effect in comparison with the sweeping velocity decrease due to no significant feature in flow structure at this time in Figure 3.10. With the sequential images, the current study also doesn't find any significant changes in flow structures, in order to re-generate the aerodynamic force after the middle of stroke. Therefore, the pitching-up effect may be displayed for a while even though the sweeping velocity keeps decreasing.

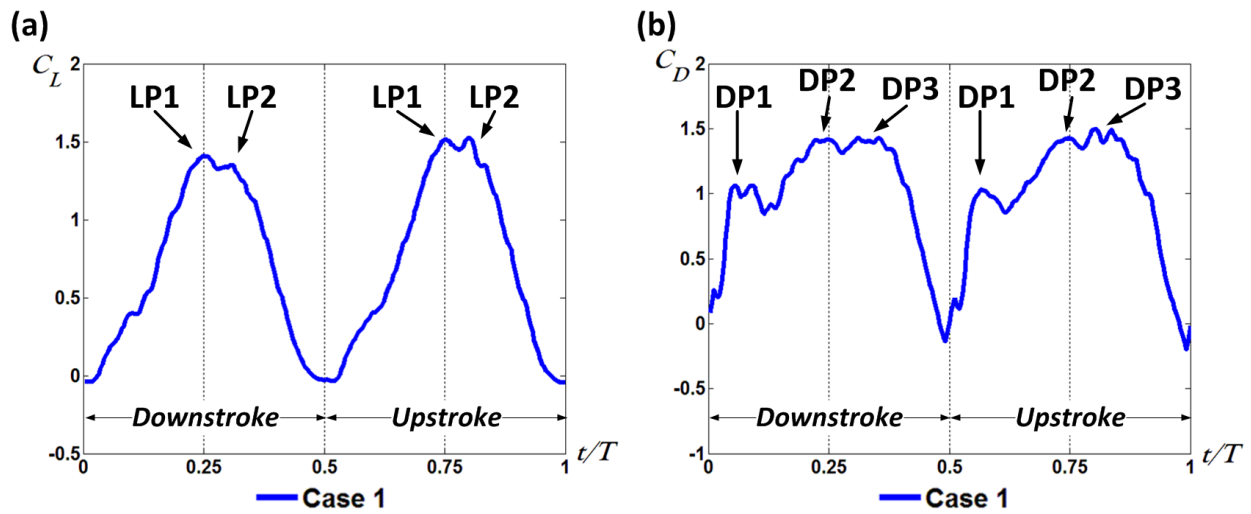


Figure 3.9 Lift and drag coefficient distributions of case 1 in a sinusoidal flapping motion

The drag coefficient has a steep increase after wing reversal as shown in Figure 3.9 (b) DP1. The rotating velocity (red, dash-line in Figure 3.8) decreases while the sweeping velocity increases after the start of stroke. In addition, the wing moves forward relatively fast with high angle of attack right after the wing reversal. It causes the first step peak in the drag coefficient. After the first step peak of drag coefficient, the drag decreases and subsequently increases again due to the sweeping velocity increase until the middle of stroke. Therefore, the second peak (DP2) is indicative around the highest sweeping velocity. Furthermore, the drag coefficient keeps increasing after the middle of stroke until the third peak (DP3). It is also due to the dominant effect of pitching-up motion over the wing velocity decrease, like the second peak in the lift coefficient.

The sinusoidal flapping motion is symmetrical so no significant difference in the vortex structures is found between downstroke and upstroke even though little differences in lift and drag coefficients exist as shown in Figure 3.9. Therefore, Figure 3.10 shows the DPIV results at 0.5R chordwise cross-section of case 1 in the sinusoidal flapping motion, and it describes the velocity vector field and the vorticity distributions at $t/T = 0.056, 0.1, 0.25, 0.304,$ and 0.55 .

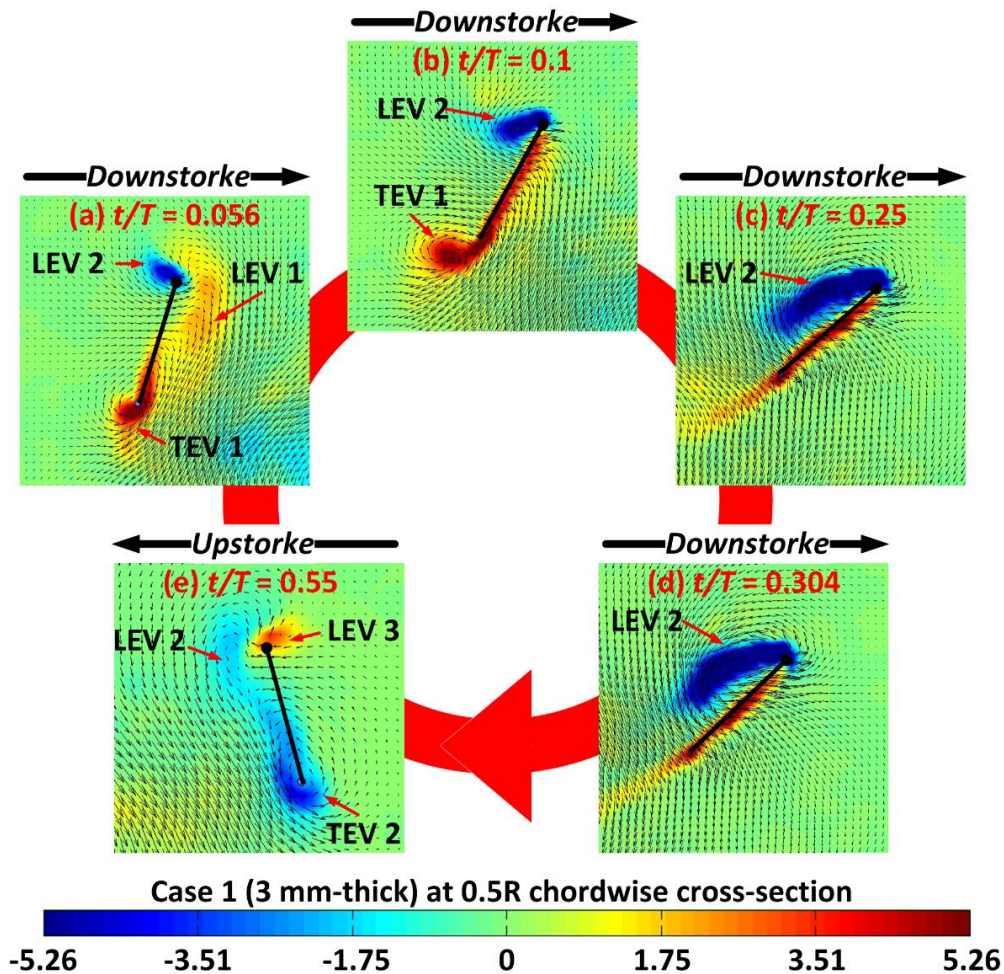


Figure 3.10 Time-resolved flow structures of case 1 at 0.5R chordwise cross-section in a sinusoidal flapping motion: (a) $t/T = 0.056$, (b) $t/T = 0.1$, (c) $t/T = 0.25$, (d) $t/T = 0.304$, (e) $t/T = 0.55$

LEV 1, which was generated for previous upstroke, is going down under the wing and LEV 2 is generated and growing from the start of stroke as shown in Figure 3.10 (a) $t/T = 0.056$. After wing reversal, the LEV 1 is still attached to the wing surface, but it seems to be weak and diffused

under the wing. When the wing starts on the downstroke, the LEV 1 loses form and finally disperses from the trailing edge. TEV 1, called a starting vortex, also starts to be generated at around $t/T = 0.056$. Both LEV 2 and TEV 1 grow as sweeping and rotating the wing from the start of downstroke, and they start to be shed for rotating the wing. However, the LEV 2 is reattached on the wing so that a stall can be delayed, which is called ‘delayed stall’. The TEV 1 is shed from the trailing edge before $t/T = 0.1$, and the LEV 2 keeps growing with increase of the aerodynamic force. The LEV 2 is going down under the wing for the wing reversal as shown in Figure 3.10 (e) $t/T = 0.55$, and it will act like the LEV 1 at $t/T = 0.056$. These PIV results have a good agreement with the past studies [39, 50].

In the symmetrical flapping motion in Figure 3.5, wing model rotates in a short period of time ($t/T_\alpha = 0.2$) when reversing the wing, thereby TEV generated by the wing reversal is close to the wing. After the wing reversal, LEV, generated by the wing reversal, with the TEV causes the wake to influence the wing. This wake arises the lift augmentation right after the wing reversal. However, the wing model in the sinusoidal flapping motion rotates gradually for pitching-up after the middle of stroke. Although TEV is generated by rotating the wing, the TEV is already far from the wing right after the wing reversing in Figure 3.10 (e). Therefore, there is no lift augmentation after reversing the wing in the sinusoidal flapping motion (Figure 3.9).

3.2 Flexible wings

3.2.1 Symmetrical flapping motion

Flexible wings in this experiment are made of the PC sheets using the CNC machine so the flexible wings do not have the veins to sustain the forms of thin wings with high flexibility. Therefore, the current study is able to observe the pure effects of wing flexibility on aerodynamic characteristics, without considering the effect of veins. Figure 3.11 shows the distributions of lift and drag coefficients for rigid wing (case 1) and flexible wings (case 2 to 8) in the symmetrical flapping motion. These results can be divided into three parts as aerodynamic force generation and flow structures: (a) almost rigid wing: case 1 and 2 (3 and 2 mm-thick), (b) flexible wings with high aerodynamic efficiency: case 3 and 4 (1 and 0.8 mm-thick), (c) flexible wings with low aerodynamic efficiency: case 5 to 8 (0.5, 0.35, 0.2 and 0.1 mm-thick).

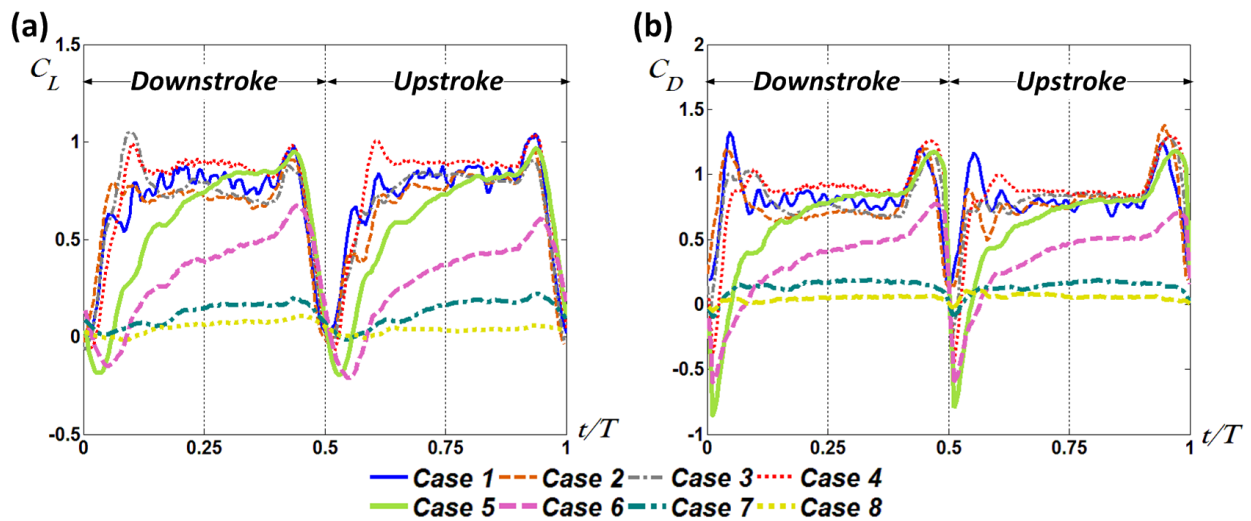


Figure 3.11 Time-resolved lift and drag coefficient distributions, from case 1 to case 8, in a symmetrical flapping motion

First, lift and drag coefficients of case 2 (orange, thin dash-line) are similar to those of case 1 (blue, thin solid-line). Case 2 shows a first step peak in drag coefficient as well as dual peaks in lift coefficient after the start of stroke. Along with the flow structures of case 1 in Figure 3.5,

case 2 has similar flow structures so this thesis does not show the PIV results of case 2. On the other hand, case 3 (gray, thin dash-dot-line) and 4 (red, thin dot-line) do not show dual peaks but one great peak in lift coefficient after the wing reversal. Additionally, their first steep peaks in drag coefficient decrease while their first steep peaks in lift coefficient increase. Figure 3.2 shows the mean lift and drag coefficients each case in the symmetrical flapping motion. Aerodynamic forces of case 3 and 4 re-increase from case 2 but no significant difference between their flow structures is measured even though their aerodynamic forces are slightly different. The flow structure of case 3, therefore, is not measured in this experiment.

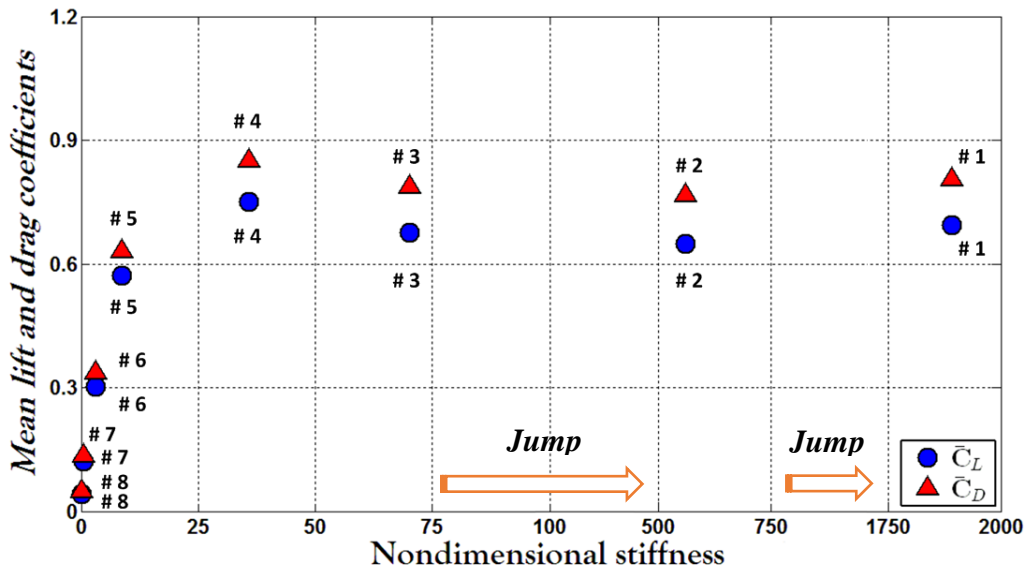


Figure 3.12 Mean lift and drag coefficients from case 1 to 8 in a symmetrical flapping motion

Case 5 to 8 demonstrate that the aerodynamic force is growing less as the wing stiffness decreases in Figure 3.12. Their aerodynamic forces are remarkably less than case 1 to 4, and besides the start-times to increase the aerodynamic force are outstandingly delayed in comparison with case 4. The delayed time is caused by the delayed-motion of the flexible flapping wings. As the wing becomes more flexible, the flexible wings don't have enough stiffness to sustain the fluid

flow for flapping wings. The flexible wings are bending and twisting so the delayed motion arises for flapping. Furthermore, the wing models of case 7 and 8 are too flexible to measure the aerodynamic force precisely. Although case 7 and 8 show the trend to deteriorate the aerodynamic force as the flexibility, it is difficult for the flapping motion to generate the measured forces of case 7 and 8. The force data of case 7 and 8 are measured around the sensor's measuring part, not on the whole wing due to the excessively bending and twisting wings. In other words, the forces, affected materially to the wing for flapping, decrease remarkably by the big wing deformation. From this cause, it is difficult to bring the measured force data and PIV results of case 7 and 8 to the current experimental results. Based on the above results, this thesis focuses a discussion on four cases (case 1, 4, 5, and 6) and their lift and drag coefficients also are redrawn in Figure 3.13. In addition, Appendices B. i. shows the distributions of lift and drag coefficients each case comparing with case 1.

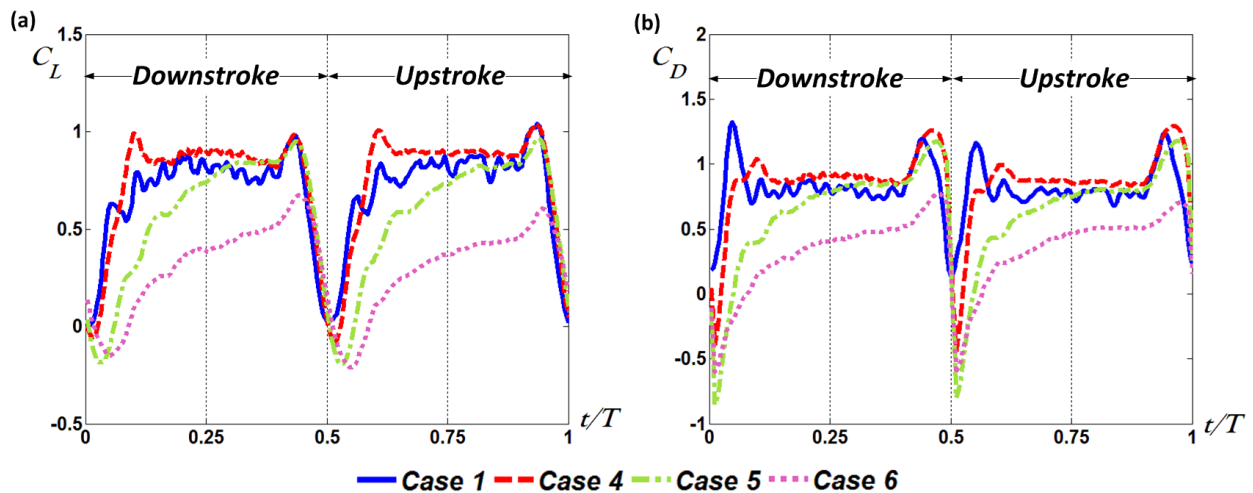


Figure 3.13 Distributions of lift and drag coefficients for case 1, 4, 5, and 6 in a symmetrical flapping motion

Some researchers [17, 18, 36, 47, 53] emphasized that the wing deformations including spanwise bending, twist, and camber of the flexible wing play an important role to influence the aerodynamic force and flow structures through computational and numerical methods. For

instance, Liu et al. [53] presented that a delay of the breakdown of leading-edge vortex for the flexible wing leads to strengthen the LEV and vortex ring in comparison with the rigid wing. Along with the breakdown-delay, phase delays in the angles of attack (α) along leading edge enhances the production of vertical aerodynamic force. Nakata and Liu [17] showed that the rotating angle (α) is advanced and the sweeping angle (ϕ) is delayed for flapping flexible wing. They presented that this wing deformation enhances the production of aerodynamic force for flapping wing. In present study, Figure 3.14 shows what motion-differences between the rigid wing (case 1) and the flexible wings (case 4, 5, and 6) are occurred at $t/T = 0.05$ and 0.25 in the symmetrical flapping motion. While the rigid wing is captured at $0.5R$ chordwise cross-section, other flexible wings are twisting and bending so the captured sections are different from the rigid wing.

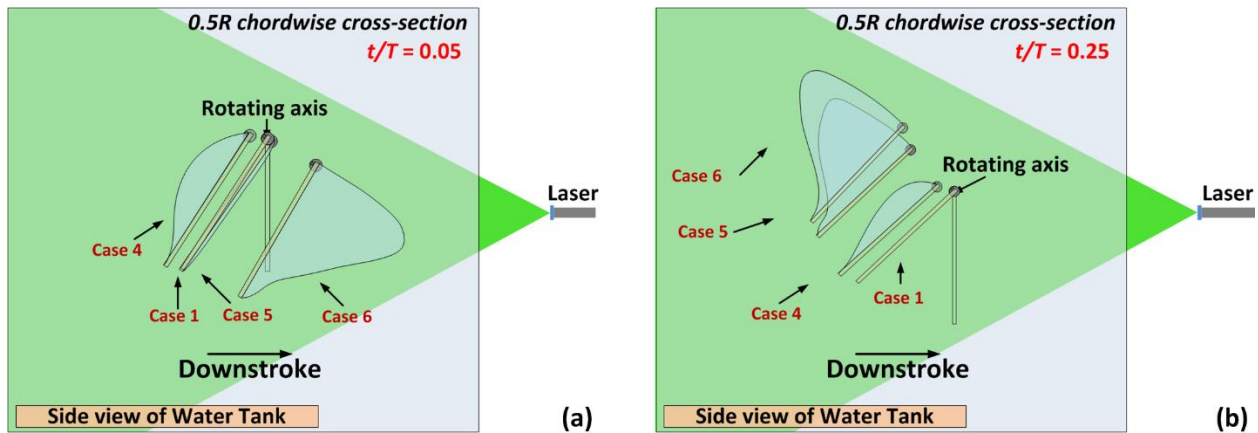


Figure 3.14 Sketches of side views for $0.5R$ chordwise cross-sectional DPIV test in a symmetrical flapping motion; (a) at $t/T = 0.05$ (b) at $t/T = 0.25$

In Figure 3.14 (a) $t/T = 0.05$, the wing cross-section of case 4 is located behind the position of case 1 (rigid wing) and them of case 5 and 6 are located in advance of rigid wing. The wings in case 5 and 6 cause the delay in rotating the wing due to their high flexibility. The delays in reversing and rotating the wing must generate different flow structures in comparison with case 1; it will be discussed in DPIV results. Moreover, the wing cross-section of case 6 still moves in the

opposite direction of downstroke unlike other cases although wing root of case 6 was already reversed.

In Figure 3.14 (b) $t/T = 0.25$, the wings in case 1, 4, 5, and 6 move in the same direction but the wing deformations still present big differences at the middle of downstroke ($t/T = 0.05$). The wing models come up during the downstroke as the wings become more flexible. Simultaneously with spanwise bending, the twist also causes the change of angles of attack. Unlike the computational methods such as previous studies [17, 18], it is hard to measure exactly how much delay of phase for the flexible wing arises numerically in flapping flights. However, it is undoubtable for flexible wings to cause the changes of sweeping and rotating angles for flapping via the sequential images observed from a high speed camera.

The symmetrical flapping motion has no significant difference in the vortex structures between the downstroke and upstroke although the lift and drag coefficients each stroke are slightly different. As previous chapter, DPIV tests take the images at same chordwise cross-section of $0.5R$ as the rigid wing. In addition, four capture points are chosen for DPIV tests each stroke: $t/T = 0.05, 0.1, 0.25, 0.45$ for downstroke, according to the above aerodynamic characteristics. Figure 3.15 illustrates the time-resolved DPIV results to describe the velocity vector field and the vorticity distributions at $0.5R$ chordwise cross-section in the symmetrical flapping motion.

As noted earlier in this thesis, the lift generation is delayed as the wing becomes flexible and leading edge vortex after the wing reversal is related to generating the lift. In Figure 3.15, the generation of LEV 2 is delayed as the thickness of the wing becomes thinner. While case 1 already forms LEV 2 at $t/T = 0.05$, case 4 starts to generate LEV 2 and case 5 and 6 do not show the generation of LEV 2 at this time. Considering the amount of time required to generate the lift in Figure 3.13, it can be proved that the LEV 2 is related to generate the lift. The delay in time to

form the LEV 2 causes the delay in time to increase the lift in general. Furthermore, the size of LEV 2 has an effect to increase the lift and besides the size decreases depending on the delayed generation of LEV 2. Compared with case 1, Figure 3.15 presents that the flexible wings have small size of LEV 2 at $t/T = 0.25$. In addition, Figure 3.13 (a) also shows that the lift in flexible wings (case 4, 5, and 6) is smaller than the lift in rigid wing (case 1) at $t/T = 0.25$.

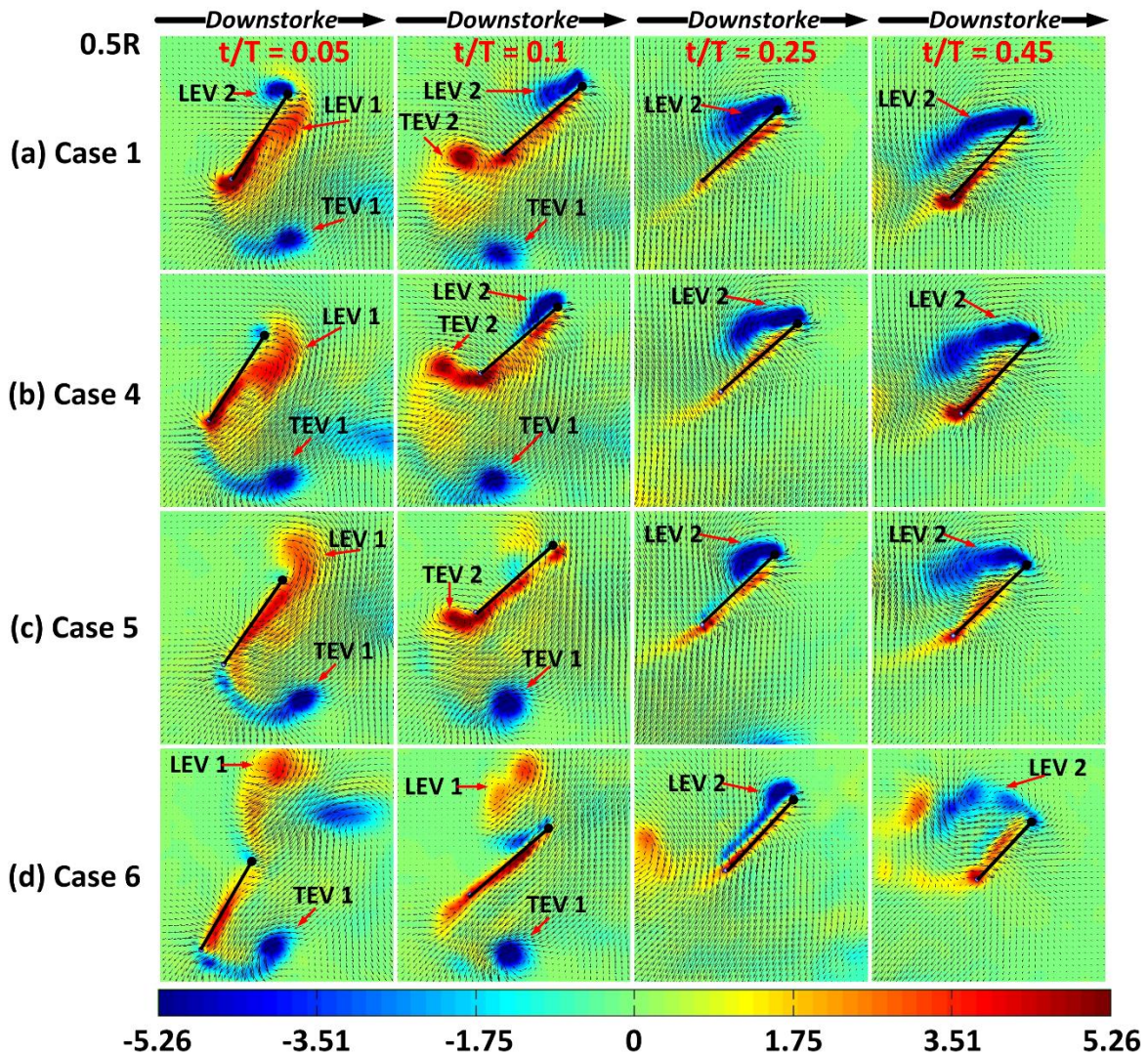


Figure 3.15 Time-resolved flow structures at 0.5R chordwise cross-section in a symmetrical flapping motion: (a) at $t/T = 0.05, 0.1, 0.25, 0.45$

The important point in the symmetrical flapping motion is the wing-wake interaction after the wing reversal. In the rigid wing (case 1), LEV 1 generated by previous stroke is attached under

the wing in the new stroke and TEV 1 is generated close to the wing during the process of reversing the wing. The attached LEV 1 and the TEV 1 indicates that the wake between the vortices induces the flow velocity increase toward the wing. This induced velocity increases with LEV 2 generation causing the lift augmentation right after the wing reversal. In flexible wings, case 4 shows the wing-wake interaction even if the time of its occurrence is a little later than case 1. The time in the wing reversal is delayed due to the delayed-motion of the flexible wing, and especially the hind wing is reversed later than the fore wing. The delayed hind wing generates TEV 1 late, so the influence of the wing-wake interaction in case 4 arises later than case 1.

After the steep augmentation of lift in the rigid wing, the lift decreases and re-increases due to the sweeping velocity increase. However, case 4 doesn't show the lift decline right after the first peak. Case 4 keeps the lift increase until the sweeping velocity is constant from $t/T = 0.1$. With the sweeping velocity increase, LEV 2 in Case 4 starts to generate from $t/T = 0.05$ as shown in Figure 3.15 (b) so the generation of LEV 2 causes the ever-increasing lift until $t/T = 0.1$. On the other hand, the drag in case 4 has lower first peak than case 1. As stated above, the effect of the wing-wake interaction in case 4 is less than the rigid wing so the induced flow towards the wing is weakened. In addition, the angle of attack relatively increases due to the bending and twisting wing. Therefore, the first steep peak of the drag coefficient in case 4 declines expectably as shown in Figure 3.13 (b).

Case 5 and 6 show different flow structures during the wing reversal in comparison with previous cases. Figure 3.15 (c) and (d) describe that LEV 1 disperses above the leading edge, not going down under the wing. The wings with high flexibility are elevated higher than case 1 and 4 for flapping. As replaying the sequential images in case 5 and 6, the wings are going down suddenly for the wing reversal so they generate vortices on high. Therefore, LEV 1 is located

above the wing after the wing reversal and the wing loses the effect of the wing-wake interaction to cause the steep increase. In addition, the wing in case 6 generates LEV 2 too late due to the delayed-motion with the distribution of LEV 1 on the wing. The delay in the LEV 2 generation and the small size of the LEV 2 also cause the low lift in case 5 and 6. Consequently, the wing-wake interaction is not acted without LEV 1 even if all cases generate TEV 1 for the wing reversal.

Based on above aerodynamic characteristics and flow structures, specific wing flexibility (in this thesis, case 4 with thickness of 0.8 mm) generates more aerodynamic force than rigid wing. In addition, the wing with high flexibility is too bending and twisting to generate the stable vortex structure. LEV 2 in case 5 and 6 disperses earlier than case 1 and 4 as shown in Figure 3.15 $t/T = 0.45$, and the wing-wake interaction occurred by the induced flow between LEV 1 and TEV 1 is not measured in case 5 and 6. It presents that the wings with high flexibility are not suitable to develop the insect-inspired flapping MAVs with better aerodynamic force to overcome their weight.

3.2.2 Sinusoidal flapping motion

Lua et al. [39] demonstrated that the distributions of aerodynamic force decreased as the wing became more flexible in a sinusoidal flapping motion. However, the current study found that specific range of wing thickness is able to generate more aerodynamic force than rigid wing. Figure 3.16 shows the distributions of lift and drag coefficients for rigid wing (case 1) and flexible wings (case 2 to 8) in the sinusoidal flapping motion. These results can also be divided into three parts like above symmetrical flapping motion: (a) almost rigid wing: case 1 and 2 (3 and 2 mm-thick), (b) flexible wings with high aerodynamic efficiency: case 3 and 4 (1 and 0.8 mm-thick), (c) flexible wings with low aerodynamic efficiency: case 5 to 8 (0.5, 0.35, 0.2, and 0.1 mm-thick).

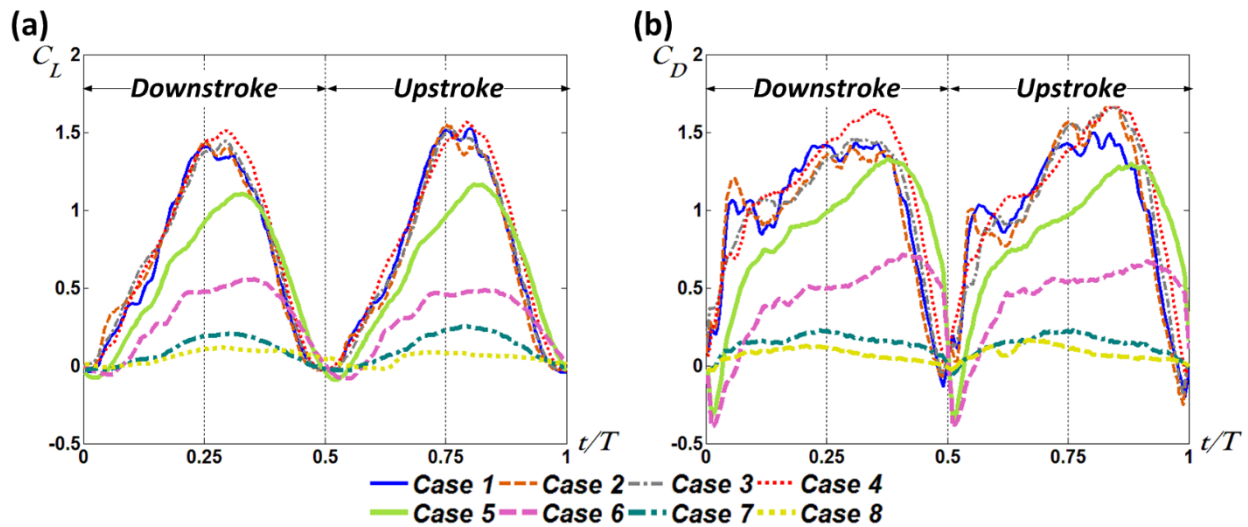


Figure 3.16 Time-resolved lift and drag coefficient distributions, from case 1 to case 8, in a sinusoidal flapping motion

Comparing case 1 with other cases, it seems to have little differences in case 1 to 4 but the dual peaks in lift coefficient and the first steep peak in drag coefficient are different. While the rigid wing (case 1) shows the dual peaks due to the pitching-up motion to overcome the sweeping velocity decrease, the lift coefficient in case 3 and 4 doesn't decrease but keeps increasing before losing the effect of the pitching-up motion. The continuous increase is generated by the similar

reason to the symmetrical flapping motion; the delayed motion arises the delay in time to generate and break-down new LEV.

In addition, the first steep peak in drag coefficient also decreases as the wing becomes flexible. Figure 3.17 shows that the aerodynamic force in case 3 and 4 is larger than case 1 and 2 and the aerodynamic force in case 5 to 8 decreases steeply comparing to previous cases. Furthermore, case 7 and 8 are not considered in this thesis by the same reason in the symmetrical motion. Therefore, the sinusoidal flapping motion also discusses only four cases, case 1, 4, 5 and 6, with their PIV results and their lift and drag coefficients are redrawn in Figure 3.18. In addition, Appendices B. ii shows the distributions of lift and drag coefficients each case comparing with case 1.

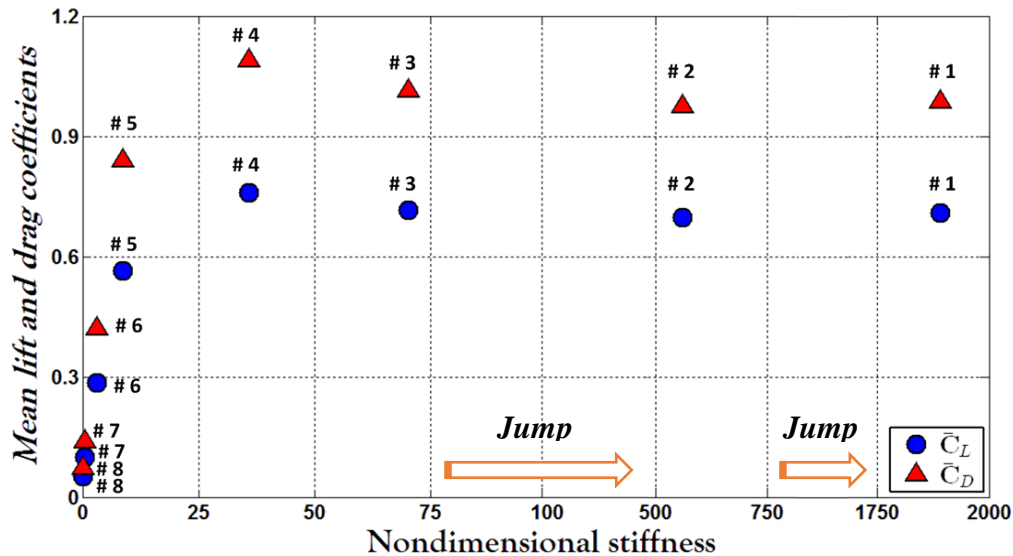


Figure 3.17 Mean lift and drag coefficients from case 1 to 8 in a sinusoidal flapping motion

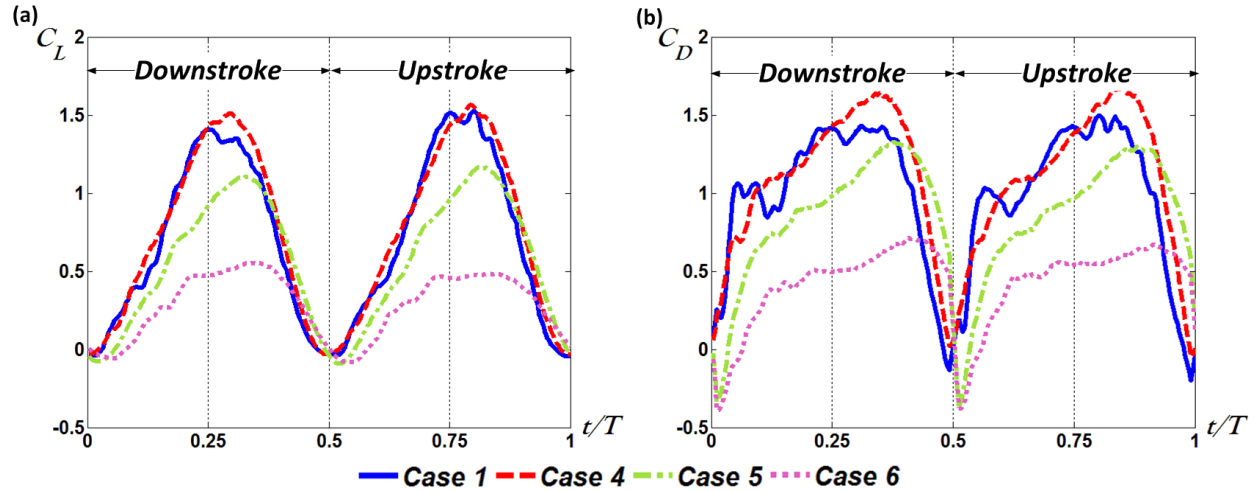


Figure 3.18 Distributions of lift and drag coefficients for case 1, 4, 5, and 6 in a sinusoidal flapping motion

In the sinusoidal flapping motion, the velocities in sweeping and rotating angles change by following the sinusoidal phase all over the stroke. Unlike the symmetrical flapping motion, the rapid changes are not expected so the wing positions have relatively less changes for the wing reversal as shown in Figure 3.19 (a). At $t/T = 0.056$, $0.5R$ cross-sections of case 4 and 5 are located behind the position of rigid wing (case 1) and that of case 6 is located in advance of rigid wing. While the wings of case 4 and 5 move in the direction of downstroke, the wing of case 6 moves in the opposite direction of downstroke even though the wing root was reversed already. This is similar to the wing motion in the symmetrical flapping motion as shown in Figure 3.14. The sinusoidal flapping motion also causes the delay in the wing rotation for the wings with high flexibility so it generates different flow structure at the trailing edge. In other words, the flow structures are also a little changed for the wing reversal in case 1 and 4. However, case 5 and 6 still show very different flow structures for reversing the wing in the sinusoidal flapping motion, due to too much bending and twisting wings.

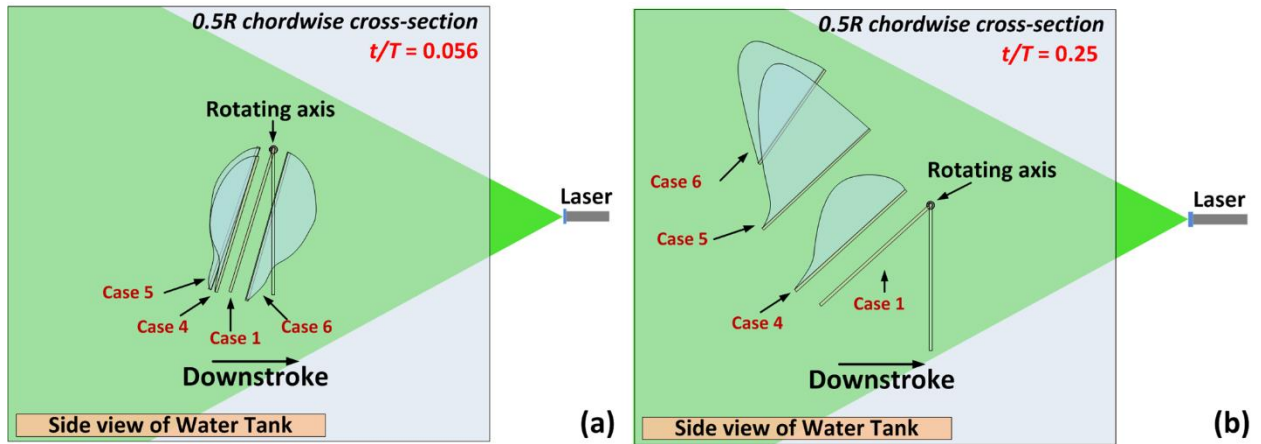


Figure 3.19 Sketches of side views for 0.5R chordwise cross-sectional DPIV test in a sinusoidal flapping motion; (a) at $t/T = 0.056$ (b) at $t/T = 0.25$

At the middle of downstroke in Figure 3.19 (b), the wings in case 1, 4, 5, and 6 move in the same direction but the wing deformations still present big differences. In addition, the wing comes up as the flexible wing have less stiffness so it indicates that, simultaneously with spanwise bending, the twist causes the change of angles of attack. The wing deformations for flapping flexible wings arise the effect to delay the aerodynamic force generation, and they also must affect the flow structures around the flapping wing. In Figure 3.16, the time to reach the highest peaks in lift and drag coefficients become delayed as the wing is more flexible.

As stated earlier, flexible wings cause the delays of flapping motion and aerodynamic force generation. Then, delay in time to reach the highest peaks occurs as the time to generate aerodynamic force is delayed. The delay of highest peak time is related to the delay of new LEV generation right after the wing reversal. Unlike case 1 and 4, case 5 and 6 present that their highest peaks in the aerodynamic force are reached too late. It expresses that the wing with high flexibility is not efficient to generate the aerodynamic force for the flapping flight. Besides, the time to generate the new LEV is too late to grow it enough to produce high aerodynamic force. The sinusoidal flapping motion is also symmetrical in each cycle although the lift and drag coefficients

each stroke are different in small. In common with the DPIV results of the rigid wing (case 1), the flow structures of flexible wings are measured at the same cross-section as the rigid wing. Figure 3.20 shows the time-resolved flow structures of case 1, 4, 5, and 6 at 0.5R chordwise cross-section. Four capture points in the sinusoidal flapping motion are a little different from the symmetrical flapping motion: $t/T = 0.056, 0.1, 0.25, 0.304$ based on the aerodynamic characteristics.

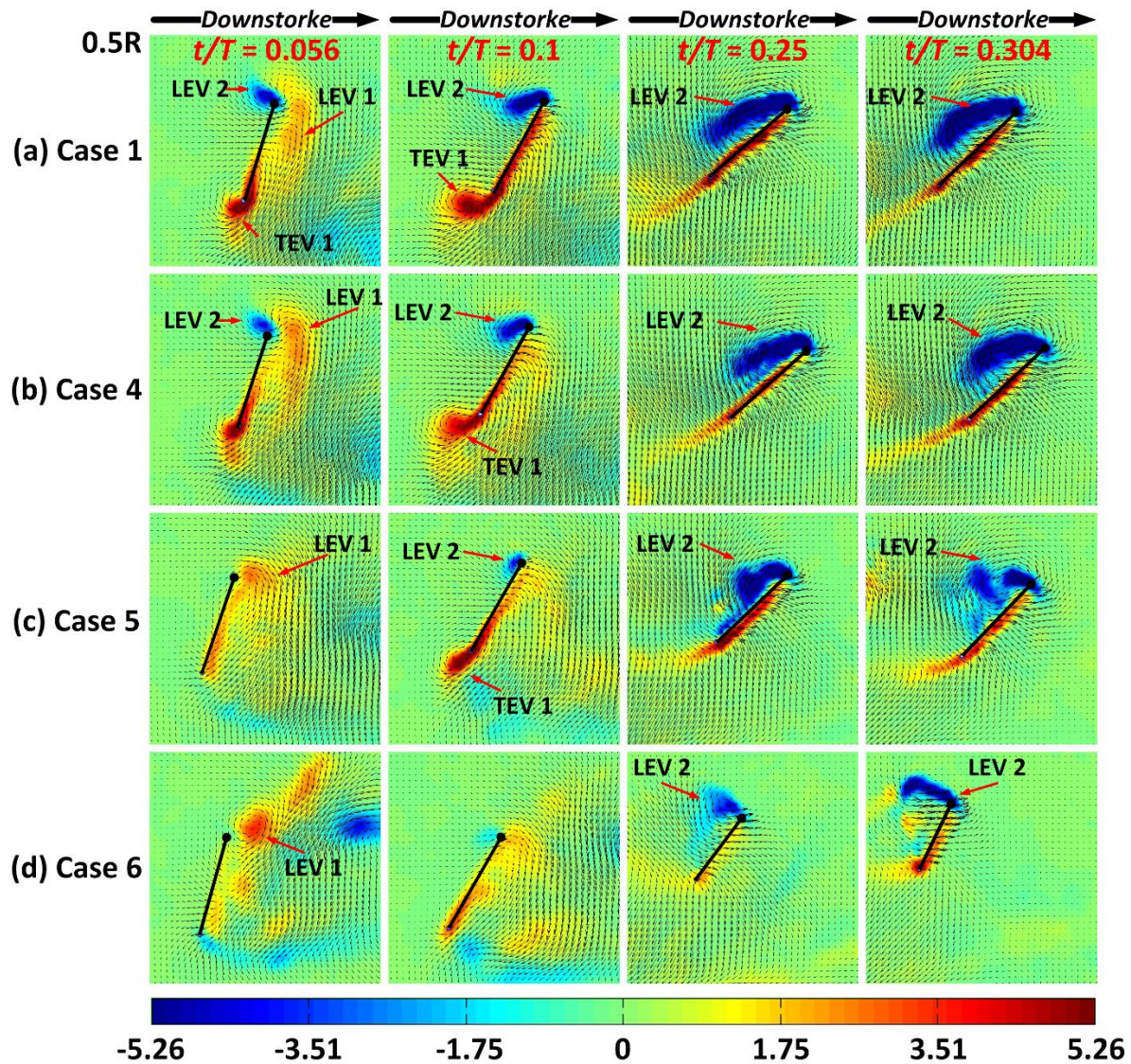


Figure 3.20 Time-resolved flow structures at 0.5R chordwise cross-section in a sinusoidal flapping motion: (a) at $t/T = 0.056, 0.1, 0.25, 0.304$

As the wing becomes flexible, LEV 1, generated by previous stroke, is not going down and its influence to the wing also declines in Figure 3.20 (a) to (d) at $t/T = 0.056$. Poelma et al. [54] and Lua et al. [39] presented that the LEV 1 is shed from the trailing edge and merges with newly TEV for reversing the wing. However, the wings with high flexibility (case 5 and 6) are bending and twisting too much so they are suddenly going down when the wing starts to be reversal.

In particular, case 6 shows that the wing rotates by following the motion of a leading edge around the wing root for reversing. Therefore, the wing is suddenly going down and new vortex, which describes LEV 1 in Figure 3.20 (d) at $t/T = 0.056$, is generated. Unlike case 1, 4, and 5, the location of LEV 1 in case 6 is above the wing and the LEV 1 partially disperses beyond the forwarding wing. Due to the dispersing LEV 1, TEV 1 is not generated yet at the captured section and simultaneously the wing is going up again for downstroke. Although TEV 1 is not shown in Figure 3.20 (d) at $t/T = 0.1$, it can be expected to generate TEV 1 late due to going down the LEV 1 late and decreasing the influence of LEV 1 under the wing.

LEV 2, which is related to generate the lift for flapping, at $0.5R$ chordwise cross-section also decreases as the wing becomes flexible in Figure 3.20. The time to generate the LEV 2 in the flexible wing is delayed so consequently the size of LEV 2 in the flexible wing becomes also smaller than the rigid wing. Figure 3.18 presents that flexible wings such as case 4 to 6 generate aerodynamic force late. The lift is reduced due to decreasing the size of LEV 2 each case. In short, the differences between their lift coefficients must be related to the generating time, the size, and breaking-down time of LEV 2 when comparing the rigid wing with the flexible wings.

In Figure 3.18 (a), case 4 has no double peaks at around the middle of stroke because the wing with specific flexibility arises less motion-delay than other wings with high flexibility. This less motion-delay causes the deceleration-delay after reaching the maximum velocity around the

middle of stroke. It seems to maintain the maximum sweeping velocity around the 0.5R chordwise cross-section even if the velocity of wing root starts to decrease right after the middle of stroke. Nakata and Liu [17] also showed that the angular velocity on sweeping angle increases earlier, then decreases later than that of the rigid wing. In the current study, sequential captured-images present that LEV 2 also keeps growing right after the middle of stroke and detaches later due to relatively the delay to rotate the wing. Therefore, the decline of the lift after the middle of stroke is not shown in Figure 3.18 (a) and the lift coefficient keeps increasing continuously.

On the other hand, LEV 2 in case 5 and 6 loses the capability to reattach to the wing for flapping. As early mentioned, the flexible wings are captured at the same chordwise cross-sections as the rigid wing so that the flexible wings actually are captured at cross-sections close to the wingtip, not exactly 0.5R chordwise cross-section. Therefore, Figure 3.20 (d) at $t/T = 0.25$ and 0.304 presents the chordwise cross-section near 70% of the wing length. Considering overall flow structures in case 5 and 6, it shows that the area of stable LEV 2 becomes growing less as increasing the flexibility. In addition to generating the LEV 2 late, the size of the LEV 2 is small and disperses easily. As shown in Figure 3.20 (c) and (d) at $t/T = 0.25$ and 0.304, the wings are going forward with relatively upper location. LEV 2 in case 5 and 6 also doesn't maintain its form at approximately 70% of the wing length. However, TEV 1 in case 5 and 6 is not existed so LEV 2 disperses only for downstroke unlike the rigid wing. The unstable flow structures show that the wings with high flexibility are not able to obtain aerodynamic force as much as insect-inspired flapping MAVs overcome their weight.

4 CONCLUSION AND FUTURE WORK

4.1 Symmetrical flapping motion vs. Sinusoidal flapping motion

Based on the previous discussions, the different features between the symmetrical flapping motion and sinusoidal flapping motion were presented through the studies of aerodynamic characteristics and flow visualizations. In the rigid wing, the symmetrical motion has the dual peaks right after the wing reversal and the last peak before reversing the wing in lift coefficient. The first dual peaks are caused by the wing-wake interaction with the generation of leading edge vortex, and the last peak is due to the dominant effect of the pitching-up motion of the wing over the wing slow-down. In drag coefficient, the first steep peak is caused by the velocity increase with a high angle of attack and the wing obtains more drag due to the wing-wake interaction. Moreover, the pitching-up motion around the end of stroke causes the last peak in the drag coefficient. In the simple harmonic motion, the rigid wing has the dual peaks around the middle of stroke in lift coefficient and the first steep peak right after the wing reversal in drag coefficient. The lift coefficient increases with the generation of LEV 2 until the maximum sweeping velocity, and the second peak is caused by the pitching-up motion. In drag coefficient, the first steep increase is caused by the velocity increase with high angle of attack. During rotating the wing, the drag decreases but re-increases with the velocity increase until the middle of stroke.

Figure 4.1 shows the flow structures of the rigid wing (case 1) in the symmetrical and sinusoidal flapping motions. The big difference between them is whether TEV generated from the previous stroke is close to the wing right after the wing reversal or not. In the symmetrical flapping motion, the wake from LEV 1 and TEV 1 induces the flow velocity increase, thereby the lift augmentation occurs right after the wing reversal. Another difference between them is the size of LEV 2. LEV 2 is very important factor to generate the lift in hovering flight. The wing in the

sinusoidal flapping motion rotates gradually and the sweeping velocity increases continuously before reaching the middle of stroke. The continuous increment makes the bigger LEV 2 than the symmetrical flapping motion as presented in Figure 4.1. Therefore, the maximum lift in the sinusoidal flapping wing is larger comparing Figure 3.12 with Figure 3.17.

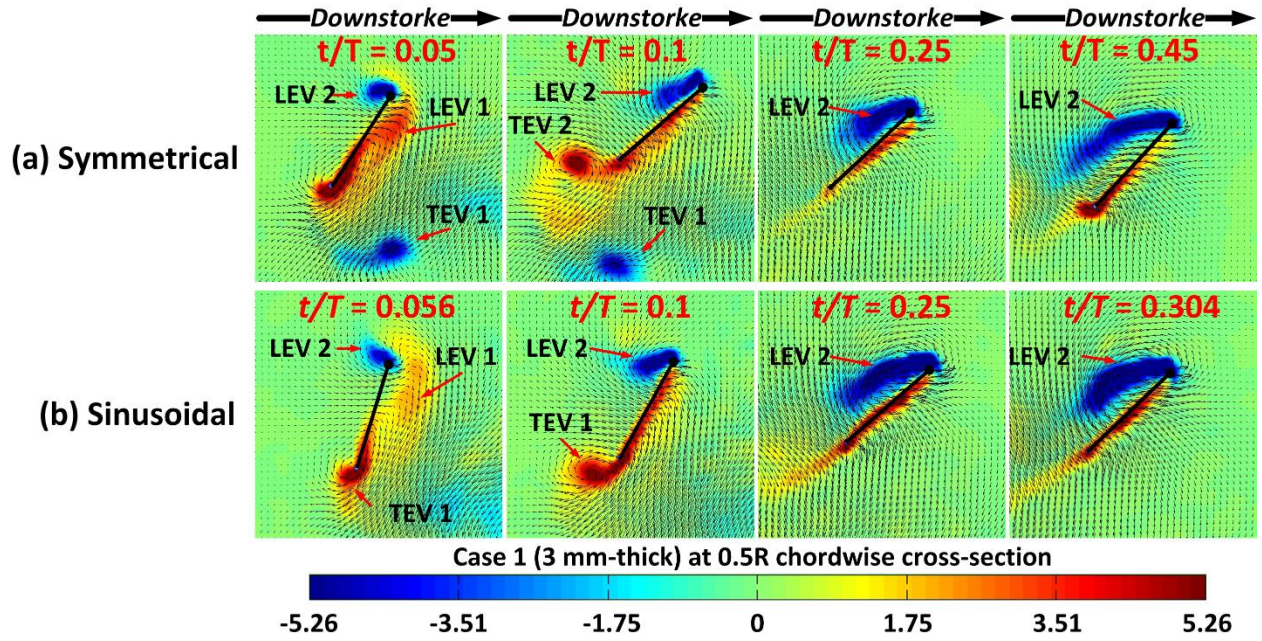


Figure 4.1 DPIV results for case 1 in both symmetrical and sinusoidal flapping motions

In flexible wings, both flapping motions present that case 4 is better than other cases to generate the aerodynamic force. This finding means that the specific range of flexibility may exist in order to obtain better aerodynamic force in hovering flight. To compare the aerodynamic efficiency, the power required (P_R) in both flapping motions is presented by using the following equation [55]:

$$P_R \propto \frac{C_L^{1.5}}{C_D} \quad (16)$$

The power required is an important factor to maintain the steady level of flight in the propulsion system. MAVs are very small and have a low velocity so they need the efficient power

consumption to obtain the aerodynamic force over their weight. When $C_L^{1.5}/C_D$ is a maximum value, the minimum power required occurs. Figure 4.2 shows $C_L^{1.5}/C_D$ from case 1 to 8 in symmetrical and sinusoidal flapping motions. Both flapping motions have the highest $C_L^{1.5}/C_D$ in case 4, but the sinusoidal flapping motion has no big difference between case 3 and 4. Moreover, the symmetrical flapping motion shows that case 5 has the similar value to case 1 and 3 so the flexible wings in case 5 is efficient enough to generate the aerodynamic force compared to the rigid wing (case 1). In all cases, the $C_L^{1.5}/C_D$ in the symmetrical flapping motion is larger than the sinusoidal flapping motion. These results describe that the symmetrical flapping motion is better to obtain high aerodynamic efficiency, and the flapping kinematics are also important point for the development of the insect-inspired flapping MAVs.

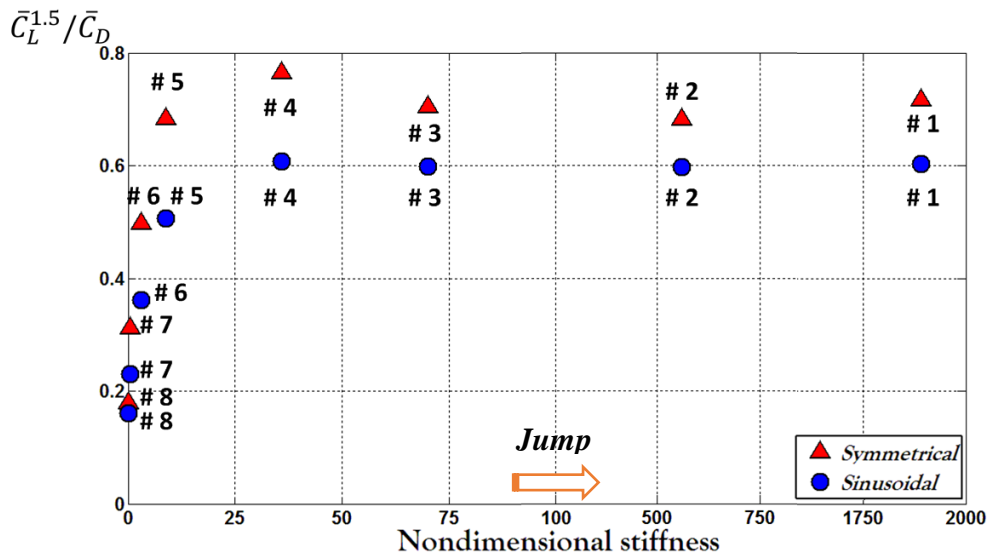


Figure 4.2 $C_L^{1.5}/C_D$, from case 1 to 8, in symmetrical and sinusoidal flapping motions

4.2 Conclusion

This study has investigated the effects of flapping hawkmoth-like wing flexibility on the aerodynamic characteristics in a symmetrical flapping motion and a sinusoidal flapping motion. The aerodynamic force generally decreases as the wing becomes flexible, but case 4 (0.8 mm-thick) has more aerodynamic force than rigid and other flexible wings. Moreover, the lift and drag coefficients of case 5 to 8 (0.5, 0.35, 0.2, and 0.1 mm-thick) decrease extremely as the wing becomes thinner. These findings present that the flexible wings have the effects on the improvement of aerodynamic force as well as on the decline of aerodynamic force. They also demonstrate that the wings with high flexibility as well as the rigid wing are unsuitable for flapping flight in MAVs.

PIV studies for flexible wing cases were not implemented experimentally in past literatures [39, 43] because of the difficulties to capture exact cross-sections, thereby the current study suggests a photographic method to capture the flexible wings on the same chordwise cross-section as a rigid wing to compare overall flow structures each case. Based on the DPIV results, this study shows that different vortex-structures undoubtedly affect the generations of aerodynamic force. Because of the bending and twisting wings, several points to generate the aerodynamic force are described in this thesis: the delay in flapping motion, the delay in time to generate vortices, and the delay to break-down/shed vortices. Each case has various flow structures via above points, and especially LEV 2 related to the lift generation presents a great difference between the cases. The flapping motion of flexible wings is delayed due to relative easy at which they bend and twist, so the flexible wings are located behind the position of rigid wing. After the wing reversal, even the wing in case 6 moves in the opposite direction to the stroke and still rotates due to the delayed-motion. The delayed transition for the flexible wings also affect the angle of attack, the induced

velocity to the wing, and the flow structures, and it causes the delay in time to generate and disperse vortices. The delayed time influences the generation of aerodynamic force, and it appears to cause the decline of aerodynamic force.

One of the main points in this experiment is the wing-wake interaction after the wing reversal. The sinusoidal flapping motion doesn't show the wing-wake interaction, generated by the TEV and LEV from the previous stroke. There is no the first steep increase right after the wing reversal in the lift coefficient. Because the TEV is already far from the wing during the wing reversal, it's not possible for only the LEV to induce the flow velocity increase as much as the steep increment. However, in the symmetrical flapping motion, the TEV from the previous stroke is close to the wing enough due to the rapid wing reversal in a short time. Therefore, the TEV and LEV after the wing reversal induces the flow to increase the flow velocity toward the wing. The induced flow influences the steep lift augmentation right after the wing reversal. Aside from this unsteady aerodynamic mechanism, the sweeping velocity increment as well as the rotational force with the LEV generation also affects the aerodynamic force in both flapping motions.

In all cases, case 4 (0.8 mm-thick) shows the increase of aerodynamic force significantly. According to the DPIV results, the wing in case 4 has a benefit to obtain more aerodynamic force from the delay in time to generate and shed vortices even though the aerodynamic force generation is a little late. While the wings with high flexibility, such as case 5 and 6, are too bending and twisting to increase the aerodynamic force, the flexibility of case 4 has an increase effect of aerodynamic force due to a little bending and twisting of the wing. The delayed-motion of case 4 overcomes the influence of velocity decrease in a sweeping direction right after the middle of stroke, so the lift coefficient increases continuously in comparison with the rigid wing. In addition, the change of angle of attack right after the middle of stroke is also delayed due to the delayed

motion so that the LEV and TEV keep on growing until the whole wing rotates and decelerates in the sweeping direction. Therefore, the aerodynamic force keeps increasing after the middle of stroke unlike the rigid wing. In the symmetrical flapping motion, case 4 has not only the benefit from the wing-wake interaction, but also the continuous LEV growth from the delayed-motion so it has better aerodynamic efficiency than other cases. The sinusoidal flapping motion also presents that case 4 has more aerodynamic force due to the delayed-motion by appropriate flexibility.

These findings demonstrate the importance of studying the flexible flapping wing in hovering flight. Also, they can motivate the researchers to look forward the range of the specific flexural stiffness for the development of Insect-inspired flapping MAVs with better aerodynamic efficiency. However, this finding is still difficult to find the specific flexibility with high aerodynamic efficiency in hovering flight. Because the flow structures are influenced by both flapping kinematics and wing flexibility, it is not easier that some specific range of flexibility is better to design the insect-inspired flapping MAVs. As previous researches [13-15, 50] have presented, flapping motion kinematics is a very important factor to obtain high aerodynamic efficiency so in the future work it is implemented for above flexible wings to obtain the high aerodynamic efficiency in similar kinematics to real flight of hawkmoth.

REFERENCE

- [1] A. Hall. (1999, June 28) Catching the Wake. *SCIENTIFIC AMERICAN*TM. Available: <http://www.scientificamerican.com/article/catching-the-wake/>
- [2] W. Shyy, Y. Lian, J. Tang, D. Viieru, and H. Liu, *Aerodynamics of Low Reynolds Number Flyers*. New York: Cambridge, 2008.
- [3] C. P. Ellington, "The Aerodynamics of Hovering Insect Flight. II. Morphological Paramters," *Philosophical Transactions of the Royal Society of London. Series B, Biological Sciences*, vol. 305, pp. 17-40, 1984.
- [4] M. Cloupeau, J. F. Devillers, and D. Devezeaux, "Direct Measurements of Instantaneous Lift in Desert Locust; Comparison with Jensen'S Experiments on Detached Wings," *The Journal of Experimental Biology*, vol. 80, pp. 1-15, 1978.
- [5] R. H. Buckholz, "MEASUREMENTS OF UNSTEADY PERIODIC FORCES GENERATED BY THE BLOWFLY FLYING IN A WIND TUNNEL," *The Journal of Experimental Biology*, vol. 90, pp. 163-173, 1981.
- [6] J. Blondeau, "Electrically evoked course control in the fly *Calliphora Erythrocephala*," *The Journal of Experimental Biology*, vol. 92, pp. 143-153, 1981.
- [7] D. L. Grodnitsky and P. P. Morozov, "VORTEX FORMATION DURING TETHERED FLIGHT OF FUNCTIONALLY AND MORPHOLOGICALLY TWO-WINGED INSECTS, INCLUDING EVOLUTIONARY CONSIDERATIONS ON INSECT FLIGHT," *The Journal of Experimental Biology*, vol. 182, pp. 11-40, 1993.
- [8] C. P. Ellington, "The Aerodynamics of Hovering Insect Flight. III. Kinematics," *Philosophical Transactions of the Royal Society of London. Series B, Biological Sciences*, vol. 305, pp. 41-78, 1984.

- [9] A. Willmott and C. Ellington, "Measuring the angle of attack of beating insect wings: robust three-dimensional reconstruction from two-dimensional images," *J Exp Biol*, vol. 200, pp. 2693-704, 1997.
- [10] A. P. Willmott and C. P. Ellington, "The mechanics of flight in the hawkmoth *Manduca sexta*. I. Kinematics of hovering and forward flight," *J Exp Biol*, vol. 200, pp. 2705-22, Nov 1997.
- [11] H. Liu, C. Ellington, K. Kawachi, C. van den Berg, and A. P. Willmott, "A computational fluid dynamic study of hawkmoth hovering," *J Exp Biol*, vol. 201 (Pt 4), pp. 461-77, Feb 1998.
- [12] C. P. Ellington, C. van den Berg, A. P. Willmott, and L. R. Thomas, "Leading-edge vortices in insect flight," *NATURE*, vol. 384, pp. 626-630, 1996.
- [13] M. Sun and J. Tang, "Unsteady aerodynamic force generation by a model fruit fly wing in flapping motion," *J Exp Biol*, vol. 205, pp. 55-70, Jan 2002.
- [14] M. Sun and J. Tang, "Lift and power requirements of hovering flight in *Drosophila virilis*," *J Exp Biol*, vol. 205, pp. 2413-27, Aug 2002.
- [15] M. H. Dickinson, F. O. Lehmann, and S. P. Sane, "Wing rotation and the aerodynamic basis of insect flight," *Science*, vol. 284, pp. 1954-60, Jun 18 1999.
- [16] R. J. Wootton, "Support and deformability in insect wings," *Journal of Zoology*, vol. 193, pp. 447-468, 1981.
- [17] T. Nakata and H. Liu, "Aerodynamic performance of a hovering hawkmoth with flexible wings: a computational approach," *Proc Biol Sci*, vol. 279, pp. 722-31, Feb 22 2012.
- [18] T. Nakata and H. Liu, "A fluid-structure interaction model of insect flight with flexible wings," *Journal of Computational Physics*, vol. 231, pp. 1822-1847, 2012.

- [19] J. Young, S. M. Walker, R. J. Bomphrey, G. K. Taylor, and A. L. Thomas, "Details of insect wing design and deformation enhance aerodynamic function and flight efficiency," *Science*, vol. 325, pp. 1549-52, Sep 18 2009.
- [20] M. H. Dickinson and K. G. Gotz, "Unsteady Aerodynamic Performance of Model Wings at Low Reynolds Numbers," *The Journal of Experimental Biology*, vol. 174, pp. 45-64, 1993.
- [21] S. P. Sane, "The aerodynamics of insect flight," *J Exp Biol*, vol. 206, pp. 4191-208, Dec 2003.
- [22] H. Liu and H. Aono, "Size effects on insect hovering aerodynamics: an integrated computational study," *Bioinspir Biomim*, vol. 4, p. 015002, Mar 2009.
- [23] S. P. Sane and M. H. Dickinson, "The aerodynamic effects of wing rotation and a revised quasi-steady model of flapping flight," *J Exp Biol*, vol. 205, pp. 1087-96, Apr 2002.
- [24] J. H. Wu and M. Sun, "Unsteady aerodynamic forces of a flapping wing," *J Exp Biol*, vol. 207, pp. 1137-50, Mar 2004.
- [25] J. M. Birch and M. H. Dickinson, "The influence of wing-wake interactions on the production of aerodynamic forces in flapping flight," *J Exp Biol*, vol. 206, pp. 2257-72, Jul 2003.
- [26] D. Kim and H. Choi, "Two-Dimensional Mechanism of Hovering Flight by Single Flapping Wing," *Journal of Mechanical Science and Technology*, vol. 21, pp. 207-221, 2007.
- [27] K. B. Lua, T. T. Lim, and K. S. Yeo, "Effect of wing-wake interaction on aerodynamic force generation on a 2D flapping wing," *Experiments in Fluids*, vol. 51, pp. 177-195, 2011.

- [28] J. Han, J. W. Chang, J. Kim, and J. Han, "Experimental study on the unsteady aerodynamics of a robotic hawkmoth *Maanduca sexta* model," in *52th Aerospace Sciences Meeting*, National Harbor, Maryland, 2014.
- [29] T. Theodorsen, "General Theory of Aerodynamic Instability and the Mechanism of Flutter," NACA1934.
- [30] L. Zhao, Q. Huang, X. Deng, and S. Sane, "The effect of chord-wise flexibility on the aerodynamic force generation of flapping wings: experimental studies," in *Robotics and Automation, 2009. ICRA '09. IEEE International Conference*, Kobe, Japan, 2009.
- [31] S. Bi and Y. Cai, "Effect of Spanwise Flexibility on Propulsion Performance of a Flapping Hydrofoil at Low Reynolds Number," *Chinese Journal of Mechanical Engineering*, vol. 25, pp. 12-19, 2012.
- [32] H. Hu, A. G. Kumar, G. Abate, and R. Albertani, "An experimental investigation on the aerodynamic performances of flexible membrane wings in flapping flight," *Aerospace Science and Technology*, vol. 14, pp. 575-586, 2010.
- [33] J. Zhang, N. S. Liu, and X. Y. Lu, "Locomotion of a passively flapping flat plate," *Journal of Fluid Mechanics*, vol. 659, pp. 43-68, 2010.
- [34] S. Ramanarivo, R. Godoy-Diana, and B. Thiria, "Rather than resonance, flapping wing flyers may play on aerodynamics to improve performance," *Proc Natl Acad Sci U S A*, vol. 108, pp. 5964-9, Apr 12 2011.
- [35] A. Gogulapati and P. P. Friedmann, "Approximate Aerodynamic and Aeroelastic Modeling of Flapping Wings in Hover and Forward Flight," in *52ND AIAA/ASME/ASCE/AHS/ASC STRUCTURES*, Denvor, CO, 2011.

- [36] M. Vanella, T. Fitzgerald, S. Preidikman, E. Balaras, and B. Balachandran, "Influence of flexibility on the aerodynamic performance of a hovering wing," *J Exp Biol*, vol. 212, pp. 95-105, Jan 2009.
- [37] H. Aono, C. Kang, C. E. S. Cesnik, and W. Shyy, "A Numerical Framework for Isotropic and Anisotropic Flexible Flapping Wing Aerodynamics and Aeroelasticity " in *28th AIAA Applied Aerodynamics Conference*, Chicago, Illinois, 2009.
- [38] M. Hamamoto, Y. Ohta, K. Hara, and T. Hisada, "Application of fluid-structure interaction analysis to flapping flight of insects with deformable wings," *Advanced Robotics*, vol. 21, pp. 1-21, 2007.
- [39] K. B. Lua, K. C. Lai, T. T. Lim, and K. S. Yeo, "On the aerodynamic characteristics of hovering rigid and flexible hawkmoth-like wings," *Experiments in Fluids*, vol. 49, pp. 1263-1291, 2010.
- [40] J. R. Usherwood and C. P. Ellington, "The aerodynamics of revolving wings I. Model hawkmoth wings," *J Exp Biol*, vol. 205, pp. 1547-64, Jun 2002.
- [41] S. A. Combes and T. L. Daniel, "Flexural stiffness in insect wings. I. Scaling and the influence of wing venation," *J Exp Biol*, vol. 206, pp. 2979-87, Sep 2003.
- [42] A. M. Mountcastle and T. L. Daniel, "Aerodynamic and functional consequences of wing compliance," *Experiments in Fluids*, vol. 46, pp. 873-882, 2009.
- [43] L. Zhao, Q. Huang, X. Deng, and S. P. Sane, "Aerodynamic effects of flexibility in flapping wings," *J R Soc Interface*, vol. 7, pp. 485-97, Mar 6 2010.
- [44] J. E. Gordon, *Structures: or Why Things Don't Fall Down*. New York: Penguin Books, 1978.

- [45] C. Kang, H. Aono, C. E. S. Cesnik, and W. Shyy, "Effects of Flexibility on the Aerodynamic Performance of Flapping Wings," *Journal of Fluid Mechanics*, vol. 689, pp. 32-74, 2011.
- [46] S. Sunada, L. Zeng, and K. Kawachi, "The relationship between dragonfly wing structure and torsional deformation," *Journal of Theoretical Biology*, vol. 193, pp. 39-45, 1998.
- [47] B. Yin and H. Luo, "Effect of wing inertia on hovering performance of flexible flapping wings," *Physics of Fluids*, vol. 22, 2010.
- [48] F. B. Tian, H. Luo, and J. Song, "Force production and asymmetric deformation of a flexible flapping wing in forward flight," *Journal of Fluids and Structures*, vol. 36, pp. 149-161, 2013.
- [49] S. N. Fry, R. Sayaman, and M. H. Dickinson, "The aerodynamics of free-flight maneuvers in *Drosophila*," *Science*, vol. 300, pp. 495-8, Apr 18 2003.
- [50] Z. J. Wang, J. M. Birch, and M. H. Dickinson, "Unsteady forces and flows in low Reynolds number hovering flight: two-dimensional computations vs robotic wing experiments," *J Exp Biol*, vol. 207, pp. 449-60, Jan 2004.
- [51] W. Shyy and H. Liu, "Flapping Wings and Aerodynamic Lift: The Role of Leading-Edge Vortices," *AIAA Journal*, vol. 45, pp. 2817-2819, 2007.
- [52] J. M. Birch and M. H. Dickinson, "Spanwise flow and the attachment of the leading-edge vortex on insect wings," *Nature*, vol. 412, pp. 729-33, Aug 16 2001.
- [53] H. Liu, T. Nakata, N. Gao, M. Maeda, H. Aono, and W. Shyy, "Micro air vehicle-motivate computational biomechanics in bio-flights: aerodynamics, flight dynamics and maneuvering stability," *Acta Mechanica Sinica*, vol. 26, pp. 863-879, 2010.

- [54] C. Poelma, W. B. Dickson, and M. H. Dickinson, "Time-resolved reconstruction of the full velocity field around a dynamically-scaled flapping wing," *Experiments in Fluids*, vol. 41, pp. 213-225, 2006.
- [55] J. D. Anderson, Jr, *Aircraft performance and design*: McGraw-Hill, 1999.

APPENDICES

A. Experimental uncertainty

In this experiment, experimental uncertainty is calculated by two sources: bias errors (B) and precision errors (P). The bias errors consist of horizontal alignment of the model and DAQ systems, and the precision errors are considered as each servo's resolution, water temperature to cause density change, and repeated-measurements with Type-A uncertainty and calibration error of 0.510204%. The bias errors have 0.00794% in horizontal alignment of the model and 0.00152% in DAQ systems. Therefore, the bias errors (B) are given by:

$$\begin{aligned}
 B &= \sqrt{\left(\frac{u(h)}{h}\right)^2 + \left(\frac{u(DAQ)}{DAQ}\right)^2} \\
 &= \sqrt{0.00794^2 + 0.0152^2} = 8.0842 \times 10^{-3}
 \end{aligned} \tag{17}$$

In the precision errors, the errors along sweeping and rotating axis are calculated as 0.0733% and 0.1163% and the errors in temperature range of 16.3 ± 0.53 °C are 0.0089%. In addition, the aerodynamic forces are measured over 250 cycles repeatedly to reduce the white noise, and the measurements start after 10 cycles in order to avoid the underdeveloped wake and the added-mass effects as Birch and Dickinson [25]. The error of these repeated measurements is 0.0338% as the following Type-A equation with standard deviation of lift data:

$$\begin{aligned}
 u(dat) &= \left(\frac{1}{n(n-1)} \sum_{k=1}^n (d_i - \bar{d})^2 \right)^{\frac{1}{2}} + u(cal) \\
 &= \left(\frac{71.1468}{250(249)} \right)^{\frac{1}{2}} + 0.510204 = 0.544
 \end{aligned} \tag{18}$$

The precision errors (P) also can be calculated by the following equation:

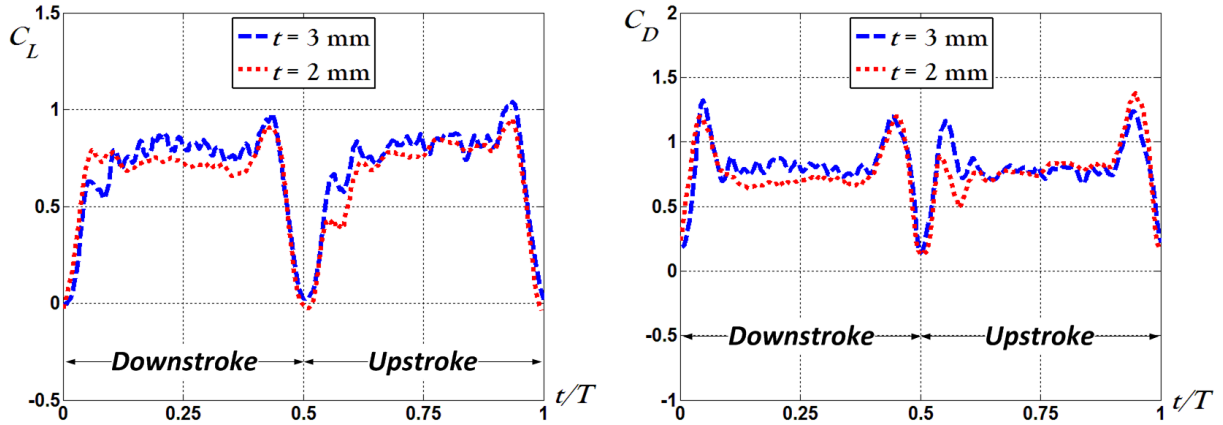
$$\begin{aligned}
 P &= \sqrt{\left(\frac{u(\rho)}{\rho}\right)^2 + \left(\frac{2u(\Phi)}{\Phi}\right)^2 + \left(\frac{2u(\alpha)}{\alpha}\right)^2} \\
 &\quad + \left(\frac{2u(\text{dat})}{\text{dat}}\right)^2} \\
 &= \sqrt{(0.020192)^2 + (2 \times 0.0733)^2 + (2 \times 0.1163)^2} \\
 &\quad + (2 \times 1.1329)^2} \\
 &= 2.2867
 \end{aligned} \tag{19}$$

Considering above bias and precision errors, the force measurement uncertainty at 95% confidence is calculated by following equation:

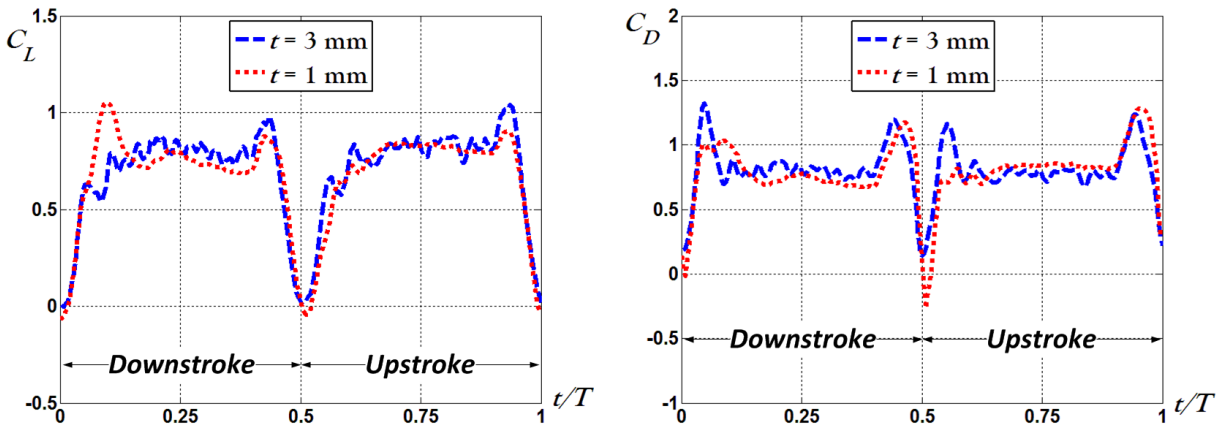
$$U(95\%) = \sqrt{B^2 + 1.96 \times P^2} = 3.195749 \tag{20}$$

B. Lift and drag coefficient

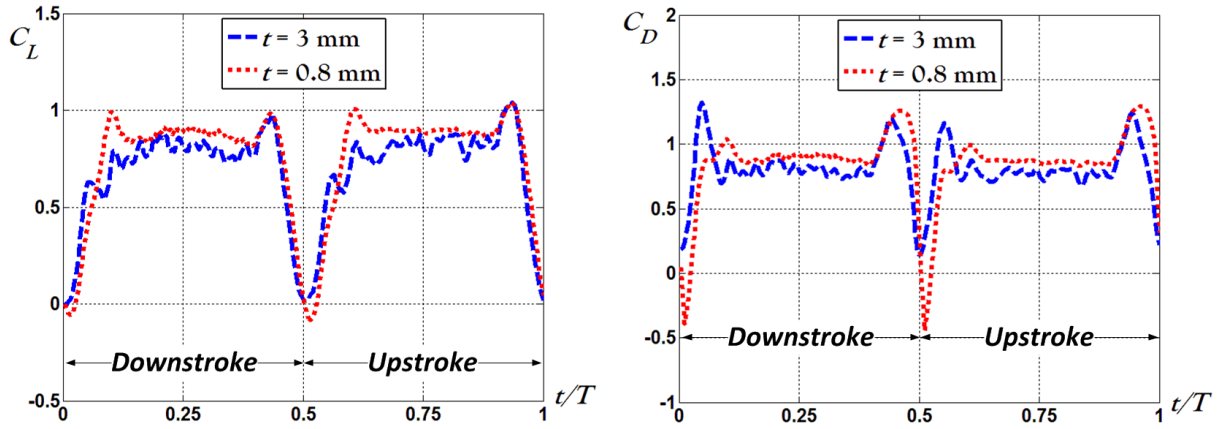
i. Symmetrical Flapping motion



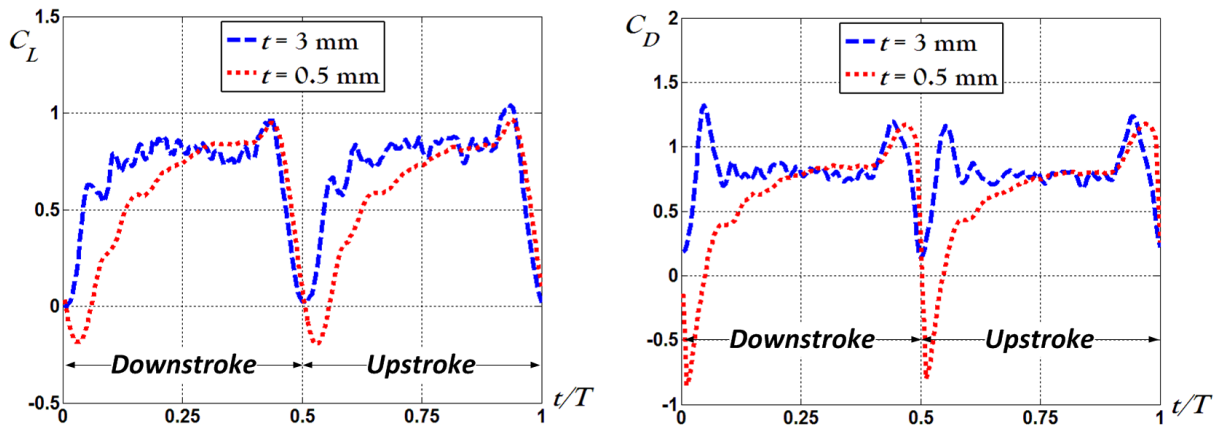
Appendix Fig. 1 Lift and drag coefficients: case 1 (3 mm-thick) vs. case 2 (2 mm-thick), in a symmetrical flapping motion



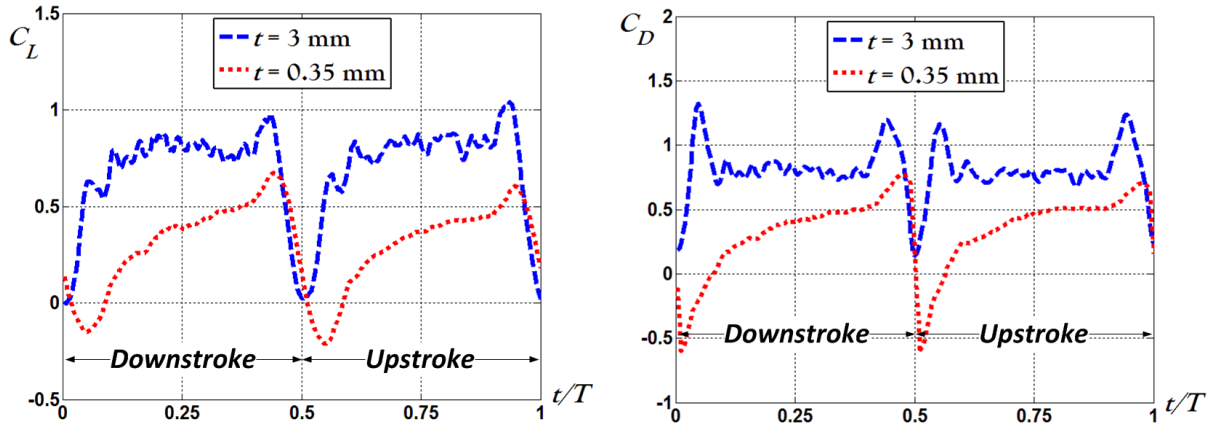
Appendix Fig. 2 Lift and drag coefficients: case 1 (3 mm-thick) vs. case 3 (1 mm-thick), in a symmetrical flapping motion



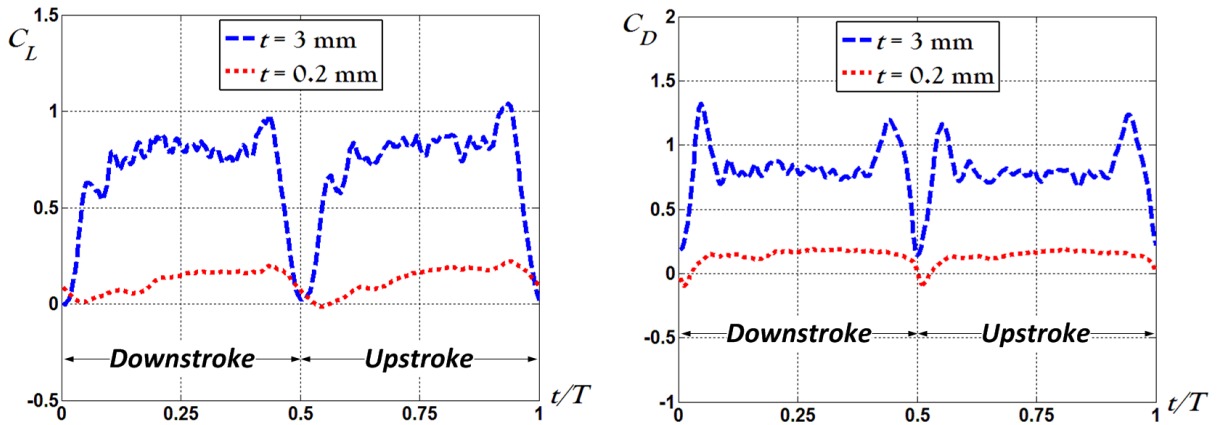
Appendix Fig. 3 Lift and drag coefficients: case 1 (3 mm-thick) vs. case 4 (0.8 mm-thick), in a symmetrical flapping motion



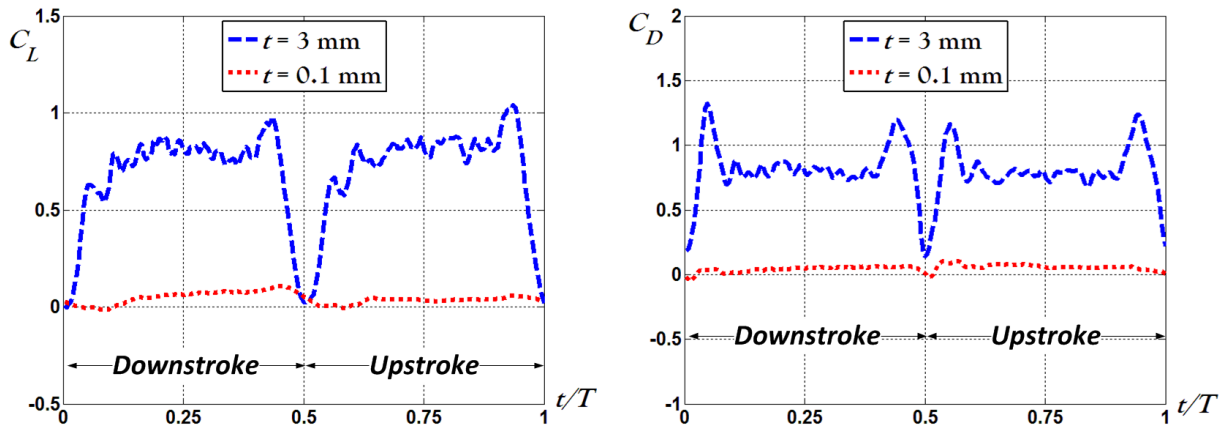
Appendix Fig. 4 Lift and drag coefficients: case 1 (3 mm-thick) vs. case 5 (0.5 mm-thick), in a symmetrical flapping motion



Appendix Fig. 5 Lift and drag coefficients: case 1 (3 mm-thick) vs. case 6 (0.35 mm-thick), in a symmetrical flapping motion

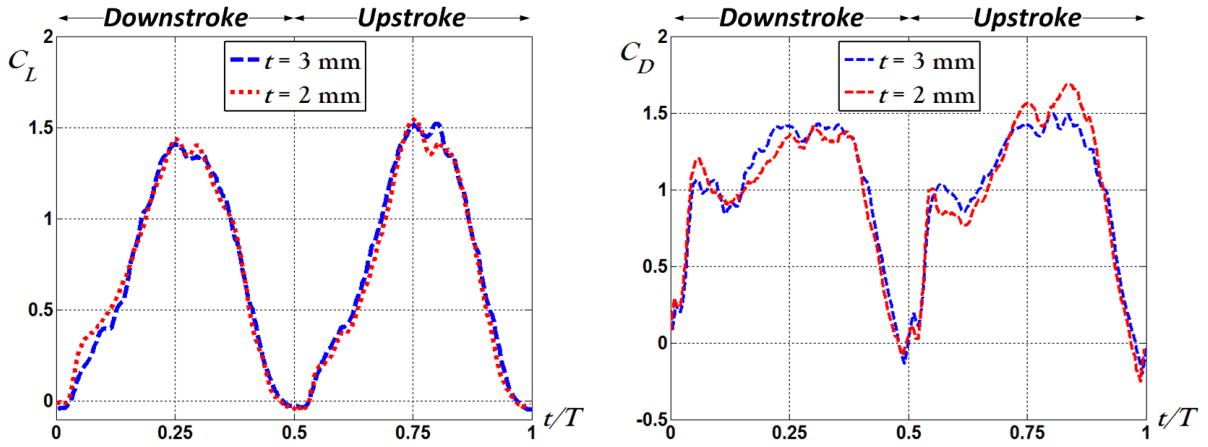


Appendix Fig. 6 Lift and drag coefficients: case 1 (3 mm-thick) vs. case 7 (0.2 mm-thick), in a symmetrical flapping motion

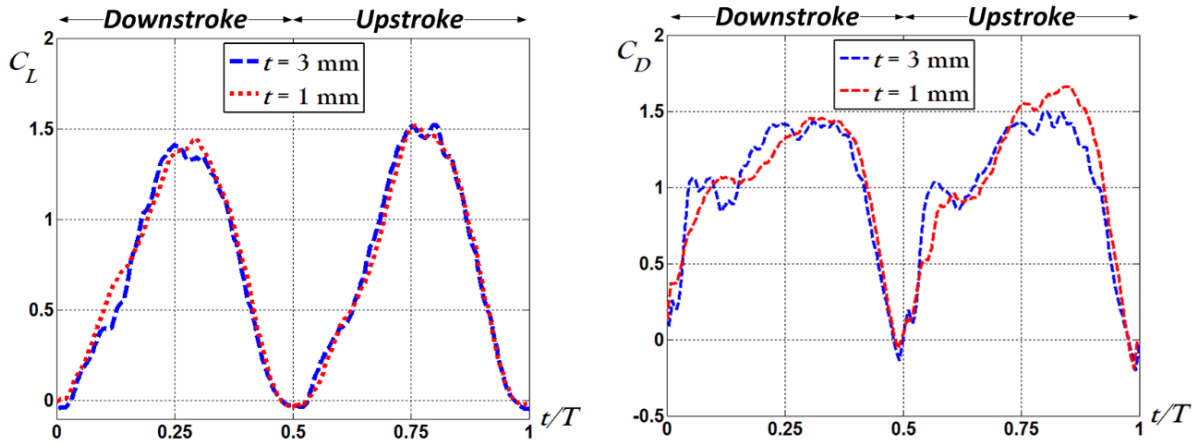


Appendix Fig. 7 Lift and drag coefficients: case 1 (3 mm-thick) vs. case 8 (0.1 mm-thick), in a symmetrical flapping motion

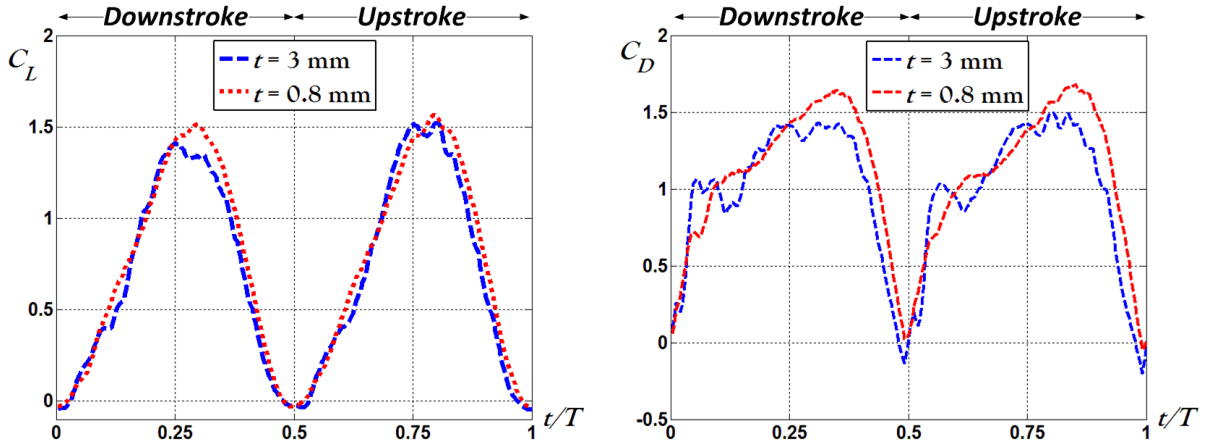
ii. Sinusoidal flapping motion



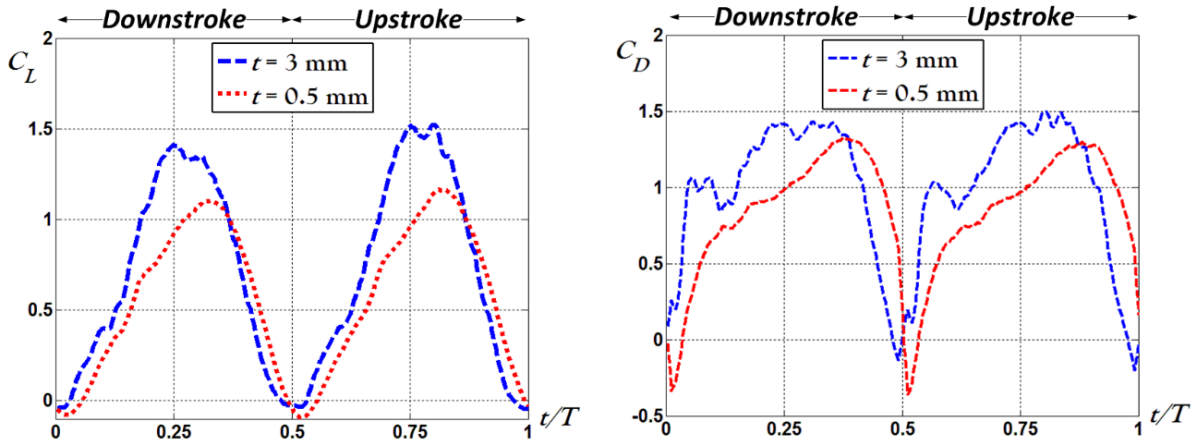
Appendix Fig. 8 Lift and drag coefficients: case 1 (3 mm-thick) vs. case 2 (2 mm-thick), in a sinusoidal flapping motion



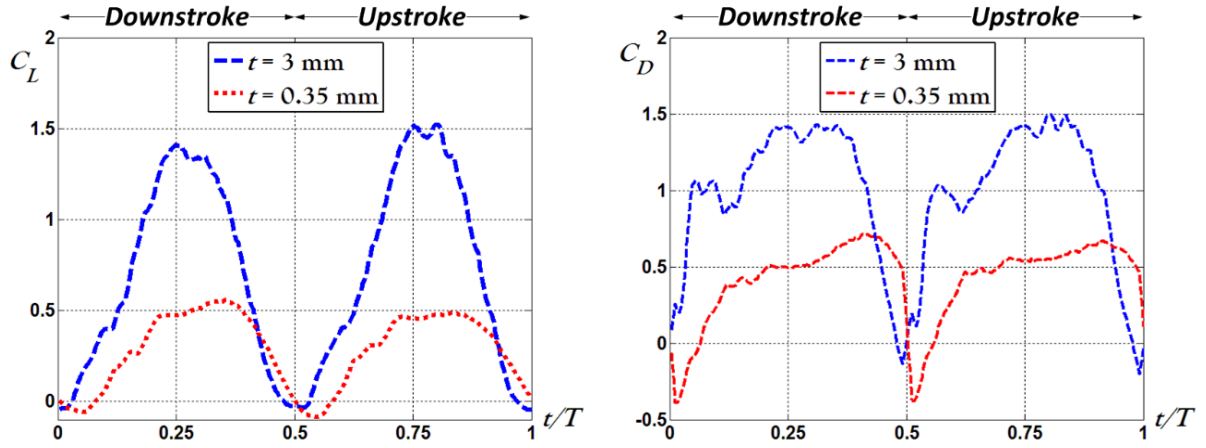
Appendix Fig. 9 Lift and drag coefficients: case 1 (3 mm-thick) vs. case 3 (1 mm-thick), in a sinusoidal flapping motion



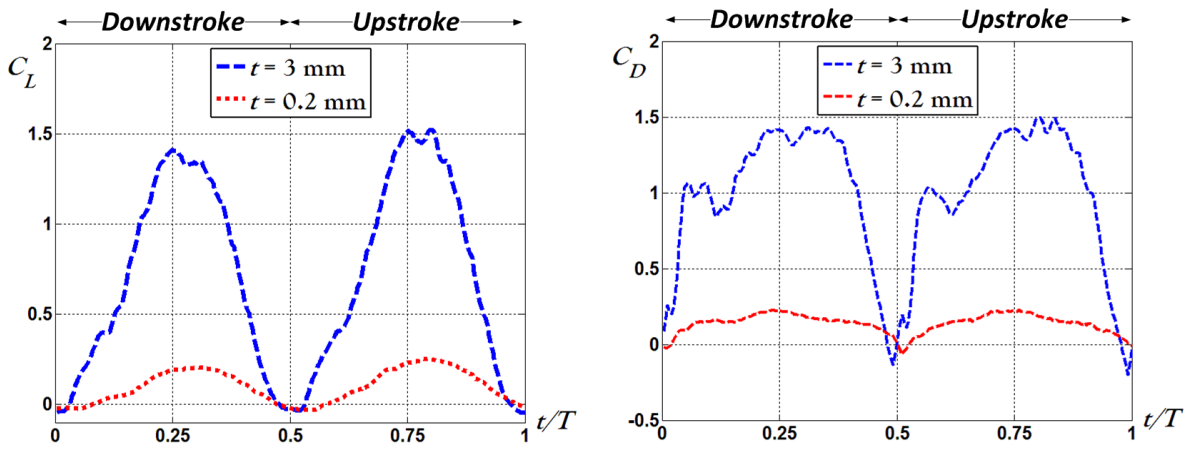
Appendix Fig. 10 Lift and drag coefficients: case 1 (3 mm-thick) vs. case 4 (0.8 mm-thick), in a sinusoidal flapping motion



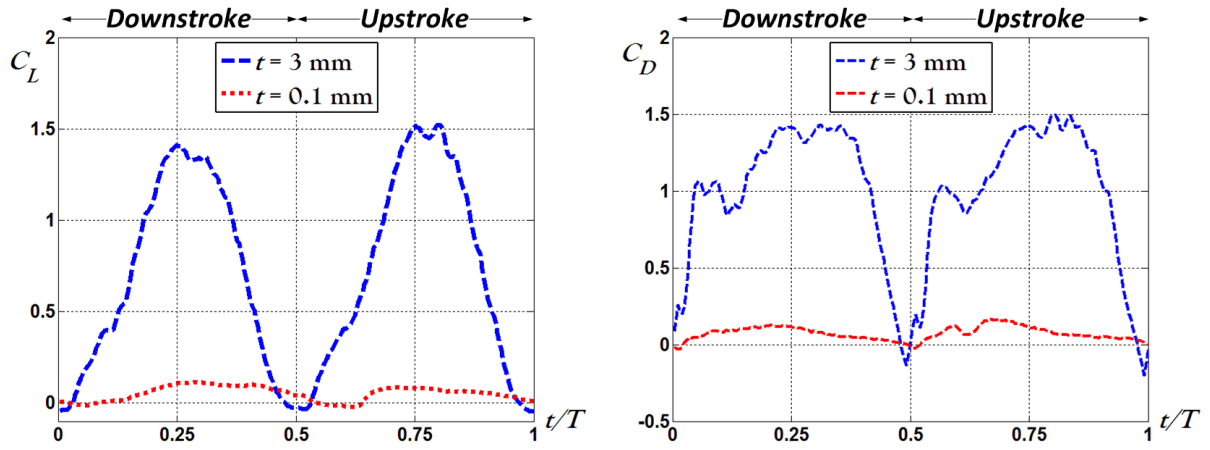
Appendix Fig. 11 Lift and drag coefficients: case 1 (3 mm-thick) vs. case 5 (0.5 mm-thick), in a sinusoidal flapping motion



Appendix Fig. 12 Lift and drag coefficients: case 1 (3 mm-thick) vs. case 6 (0.35 mm-thick), in a sinusoidal flapping motion



Appendix Fig. 13 Lift and drag coefficients: case 1 (3 mm-thick) vs. case 7 (0.2 mm-thick), in a sinusoidal flapping motion



Appendix Fig. 14 Lift and drag coefficients: case 1 (3 mm-thick) vs. case 8 (0.1 mm-thick), in a sinusoidal flapping motion